Short Papers

Analysis of a Nonconfocal Suspended Strip in an Elliptical Cylindrical Waveguide

Hassan A. Ragheb

***Abstract*—The separation of variables method along with an addition theorem of Mathieu functions are employed in this paper to analyze the problem of a nonconfocal suspended strip in an elliptical waveguide. An infinite-dimensional determinant is obtained, which represents the characteristic equation of the proposed structure. To obtain the cutoff wavenumbers for both TE and TM cases of such a structure, the infinite determinant is truncated. Convergence when truncating was observed. Numerical results for the special case of a confocal structure is discussed first for comparison with published data. Results of other interesting cases are also presented.**

***Index Terms*—Elliptical waveguide, strips.**

I. Introduction

Elliptical waveguides have been the subject of many investigations due to their wide applications in radar feed lines, multichannel communication, and accelerator beam tubes. Chu [1] presented the theory of the transmission of the electromagnetic waves in elliptical waveguide. The propagation of the electromagnetic waves in elliptical waveguide and the results of the cutoff wavelength of 19 successive modes were presented by Kretzschmar [2]. Bulley [3] introduced a theory for the analysis of an arbitrarily shaped waveguide by a polynomial approximation. This theory was improved and implemented for analyzing elliptical waveguides [4]. The fields associated with the TM_{01} mode of the elliptical waveguide were corrected by Goldberg *et al.* [5]. Recently, Zhang and Shen [6] calculated the cutoff wavelengths of the lowest 100 successive modes, as well as the curve-fitting expressions for the lowest ten-order modes.

Another line of research [7] investigated elliptical waveguide loaded with ridges or a suspended strip. It was assumed that the ridges extended from the walls to the focal points. Recently, Rozzi *et al.* [8] reported a complete analysis for a suspended strip in an elliptical cylindrical waveguide. He considered that the suspended strip extended between the focal points of the elliptical waveguide. He obtained the cutoff wavelengths for different TEM, TE, and TM modes using the separation of variables.

The objective of this paper is to extend Rozzi's analysis for the more general case of a strip of arbitrary width. The strip width could be greater or less than the focal length of the elliptic cylinder. This problem will be more general and will accommodate some important special cases such as a circular cylinder with a suspended strip.

II. Theory

Consider the two-dimensional cross-sectional geometry shown in Fig. 1. It consists of an infinitely long perfectly conducting elliptic cylinder, with focal length $2b$. A perfectly conducting strip of width $2a$ and infinite length is placed along the line joining the focal points of the elliptic cylinder such that its axes coincide with that of the elliptical waveguide. The strip width can take any value greater or less than $2b$. In order to facilitate our analysis, two elliptical coordinate systems are considered. The local coordinates (u_o, v_o, z) are at the center of the strip while the global coordinates (u, v, z) are considered at the center of the elliptic cylinder. The solution of the scalar Helmholtz wave equation in elliptical coordinates can be written as

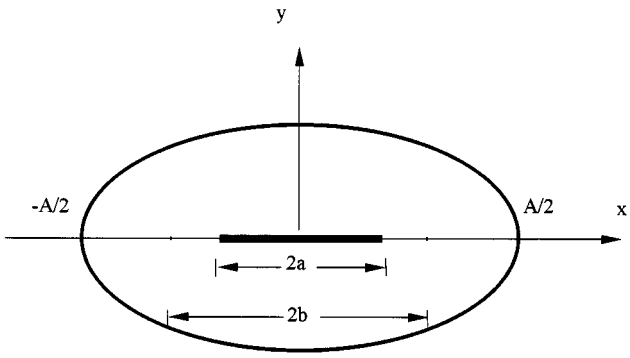

Fig. 1. Geometry of the problem.

$$\psi(\zeta_o, \eta_o) = \sum_{n=0}^{\infty} \left\{ Ae_n \, Je_n(c_o, \zeta_o) + Be_n \, Ne_n(c_o, \zeta_o) \right\} \cdot Se_n(c_o, \eta_o) e^{-j\beta z} \quad (1)$$

for the even modes, while for the odd modes, it is

$$\psi(\zeta_o, \eta_o) = \sum_{n=0}^{\infty} \left\{ Ao_n \, Jo_n(c_o, \zeta_o) + Bo_n \, No_n(c_o, \zeta_o) \right\} \cdot So_n(c_o, \eta_o) e^{-j\beta z} \quad (2)$$

where $\zeta = \cosh u$, $\eta = \cos v$, $c_o = k_c a$ ($k_c^2 = k^2 - \beta^2$, and k_c is the transverse component, while $k = 2\pi/\lambda$ is the free-space wavenumber, λ is the wavelength, and β is the propagation constant). Je_n and Ne_n are even modified radial Mathieu functions of the first and second kinds, respectively, while Jo_n and No_n are their corresponding odd functions. Se_n and So_n are the even and odd angular Mathieu functions. Ae_n, Ao_n, Be_n, and Bo_n are coefficients to be calculated by imposing the boundary conditions.

A. TE Case

These modes must satisfy the boundary condition of vanishing tangential components of the electric field ($E_v = 0$) on the perfectly conducting surfaces, i.e.,

$$\frac{\partial \psi}{\partial u_o}\Big|_{u_o=0} = 0, \qquad 0 \le v_o \le 2\pi$$

and

$$\frac{\partial \psi}{\partial u}\Big|_{u=u_k} = 0, \qquad 0 \le v \le 2\pi \quad (3)$$

where u_k = constant represents the surface of conducting the elliptic cylinder. Since we have even and odd modes in each case, one can consider them individually as follows.

Manuscript received May 1, 1998.

The author is with the Department of Electrical Engineering, King Fahd University of Petroleum and Minerals, Dhahran 31261, Saudi Arabia.

Publisher Item Identifier S 0018-9480(00)05476-4.

0018–9480/00$10.00 © 2000 IEEE

TABLE I
COMPARISON BETWEEN OUR RESULTS AND ROZZI *et al.* [8]. (a) FOR THE TM MODES. (b) FOR THE TE MODES

e		0.1	0.2	0.3	0.4	0.5	0.6	0.7	0.8	0.9
TM^s_{01}	Ours	1.0230	0.9406	0.8702	0.8074	0.7503	0.6934	0.6274	0.5394	0.4047
	Rozzi et al.	1.02	0.94	0.87	0.81	0.75	0.70	0.63	0.54	0.40
TM^s_{11}	Ours	0.8070	0.7734	0.7259	0.6704	0.6128	0.5591	0.5090	0.4498	0.3541
	Rozzi et al.	0.81	0.78	0.74	0.68	0.62	0.56	0.51	0.45	0.35
TM^e_{11}	Ours	0.8168	0.8074	0.7911	0.7671	0.7336	0.6883	0.6264	0.5393	0.4047
	Rozzi et al.	0.82	0.81	0.79	0.77	0.74	0.69	0.63	0.54	0.41

(a)

e		0.1	0.2	0.3	0.4	0.5	0.6	0.7	0.8	0.9
TE^e_{11}	Ours	1.7059	1.7049	1.7031	1.7006	1.6972	1.6930	1.6878	1.6816	1.6741
	Rozzi et al.	1.706	1.705	1.702	1.699	1.693	1.692	1.684	1.680	1.669
TE^s_{11}	Ours	1.7164	1.7493	1.8094	1.8976	2.0100	2.1402	2.2821	2.4310	2.5838
	Rozzi et al.	1.715	1.749	1.809	1.896	2.007	2.135	2.273	2.418	2.565
TE^s_{21}	Ours	1.0261	1.0190	1.0091	0.9995	0.9955	1.0028	1.0250	1.0605	1.1045
	Rozzi et al.	1.025	1.019	1.009	1.001	0.998	1.009	1.037	1.077	1.124

(b)

1) TE Even Modes: Applying the first boundary condition $(\partial\psi/\partial u_o)|_{u_o=0} = 0, \quad 0 \le v_o \le 2\pi$, one can obtain $Be_n = 0$, which, when substituting in (1), yields

$$\psi(\zeta_o, \eta_o) = \sum_{n=0}^{\infty} Ae_n \, Je_n(c_o, \zeta_o) Se_n(c_o, \eta_o) e^{-j\beta z}. \quad (4)$$

Now, in order to apply the second boundary condition, $\psi(\zeta_o, \eta_o)$ must be transferred to the global coordinate system (ζ, η). This can be done using the addition theorem of Mathieu functions [10], which is simplified for this case as

$$Rx_n(c_o, \zeta_o) Sx_n(c_o, \eta_o) = \sum_{l=0}^{\infty} Kx_{n,l} Rx_l(c, \zeta) Sx_l(c, \eta) \quad (5)$$

where Rx_n could be Je_n, Jo_n, Ne_n, or No_n, Sx_n could be Se_n or So_n; also, $Kx_{n,l}$ could be $Ke_{n,l}$ or $Ko_{n,l}$ and $c = k_c b$ while

$$Ke_{n,l} = \frac{\pi(-j)^{l-n}}{M_l^{(e)}(c)} \sum_{r=0}^{\infty} \varepsilon_r De_r^n(c_o) De_r^l(c)$$
$$\varepsilon_r = \begin{cases} 2, & r = 0 \\ 1, & \text{otherwise} \end{cases} \quad (6)$$

$$Ko_{n,l} = \frac{\pi(-j)^{l-n}}{M_l^{(o)}(c)} \sum_{r=1}^{\infty} Do_r^n(c_o) Do_r^l(c) \quad (7)$$

where $M_l^{(e)}(c)$ and $M_l^{(o)}(c)$ are normalization constants for even and odd functions, respectively, which are defined in [9]. The summation over r in (6) and (7) extends over even values of r if n is even and odd values of r if n is odd. The constants De_m^n and Do_m^n are coefficients of the infinite series of angular Mathieu functions in terms of trigonometric functions defined in [9]. To apply the second boundary condition, (5) is employed in (4) as

$$\psi(\zeta, \eta) = \sum_{n=0}^{\infty} \sum_{l=0}^{\infty} Ae_n Ke_{n,l} Je_l(c, \zeta) Se_l(c, \eta) e^{-j\beta z}. \quad (8)$$

Applying the second boundary condition and using the orthogonal property of the triangular Mathieu functions, one obtains

$$\sum_{n=0}^{\infty} Ae_n Ke_{n,l} Je_l'(c, \zeta_k) = 0. \quad (9)$$

Equation (9) can be written in the matrix form

$$[Z_{l,n}][Ae_n] = 0. \quad (10)$$

A nontrivial solution can be obtained if the determinant of the Z matrix vanishes. The solution of the resulting determinant will give the values of k_c corresponding to the first, second, . . ., and nth cutoff wavenumbers. Once the value of k_c is obtained for the ith cutoff wavenumber, the coefficients can be obtained, and the field distribution inside the waveguide is then completely defined.

TABLE II
THREE CUTOFF WAVELENGTHS FOR DIFFERENT CASES OF TM AND TE MODES

	Even TM	Odd TM	Even TE	Odd TE
a/A = 0.5 , b/A = 0.002	0.8271	0.8199	1.7063	2.2054
	0.6483	0.6117	1.0285	1.2821
	0.4440	0.4478	0.8199	0.8069
a/A = 0.1 , b/A = 0.3	0.9993	0.7911	1.7031	1.6495
	0.7981	0.5972	1.0067	1.2525
	0.5980	0.4316	0.7992	0.5831
a/A = 0.1 , b/A = 0.6	0.9018	0.6883	1.6930	1.3991
	0.7563	0.5414	0.9580	1.1453
	0.5531	0.3711	0.7054	0.5338
a/A = 0.1 , b/A = 0.9	0.6105	0.4047	1.6741	0.8385
	0.5692	0.3541	0.9144	0.4244
	0.3771	0.2101	0.6327	0.3328
a/A = 0.3 , b/A = 0.1	0.8943	0.8168	1.7059	1.8733
	0.7356	0.6102	1.0260	1.2793
	0.6002	0.4461	0.8178	0.7137
a/A = 0.3 , b/A = 0.6	0.7738	0.6883	1.6930	1.5736
	0.6816	0.5414	0.9580	1.1433
	0.5503	0.3711	0.7054	0.6263
a/A = 0.3 , b/A = 0.9	0.5179	0.4047	1.6741	1.0572
	0.5056	0.3541	0.9144	0.8366
	0.3661	0.2101	0.6327	0.4228
a/A = 0.5 , b/A = 0.1	0.8334	0.8168	1.7059	2.1980
	0.6517	0.6102	1.0260	1.2790
	0.5489	0.4461	0.8178	0.8041
a/A = 0.5 , b/A = 0.6	0.7050	0.6883	1.6930	1.9158
	0.5852	0.5414	0.9580	1.1431
	0.5115	0.3711	0.7054	0.6878
a/A = 0.5 , b/A = 0.9	0.4144	0.4047	1.6741	1.4190
	0.3853	0.3541	0.9144	0.8352
	0.3356	0.2101	0.6327	0.4344
a/A = 0.7, b/A = 0.1	0.8190	0.8168	1.7059	2.6827
	0.6152	0.6102	1.0260	1.2767
	0.4829	0.4461	0.8178	0.8433
a/A = 0.7, b/A = 0.6	0.6895	0.6883	1.6930	2.4039
	0.5386	0.5414	0.9580	1.1430
	0.4512	0.3711	0.7054	0.7051
a/A = 0.7, b/A = 0.8	0.5400	0.5393	1.6816	2.1196
	0.4414	0.4494	0.9278	0.9818
	0.3892	0.2847	0.6471	0.5493

2) TE Odd Modes: Following the same procedure described for the TE even modes, but with $\psi(\zeta_o, \eta_o)$ represented in terms of odd functions [see (2)], one ends up with a matrix equation similar to that in (10), where the elements of the matrix are given by

$$Z_{l,n} = Ko_{n,l}\left\{Jo_l'(c, \zeta_k) - \frac{Jo_n'(c_o, 1)}{No_n'(c_o, 1)} No_l'(c, \zeta_k)\right\} \quad (11)$$

and the coefficient vector is denoted as Ao_n. Again, the determinant of the matrix is equal to zero to obtain the cutoff wavenumbers.

B. TM Case

These modes must satisfy the boundary condition of vanishing tangential components of the electric field ($E_u = 0$) on the perfectly conducting surfaces, i.e.,

$$\psi|_{u_o=0} = 0, \qquad 0 \le v_o \le 2\pi$$

and

$$\psi|_{u=u_k} = 0, \qquad 0 \le v \le 2\pi. \quad (12)$$

Even and odd modes can be considered individually as follows.

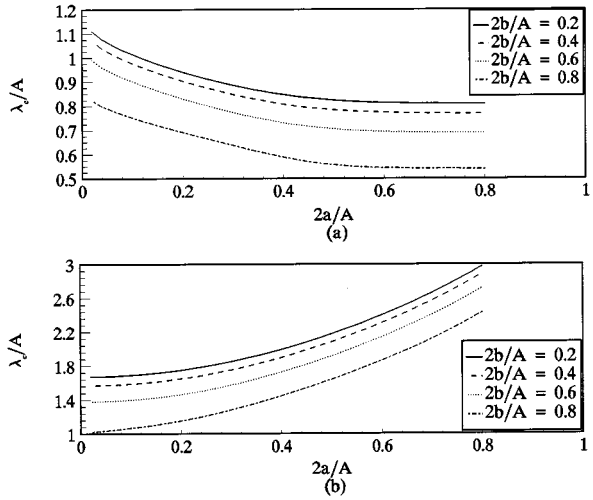

Fig. 2. First cutoff wavelength versus strip width for: (a) the even TM mode and (b) the odd TE mode.

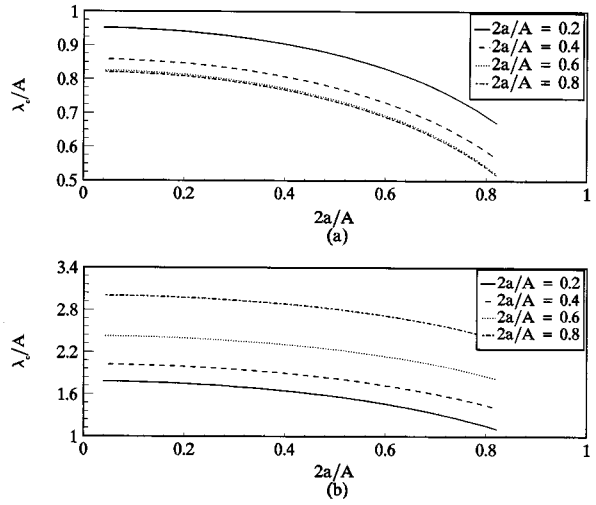

Fig. 3. First cutoff wavelength versus elliptic guide eccentricity for: (a) the even TM mode and (b) the odd TE mode.

1) TM Even Modes: Applying the first boundary condition along with the orthogonal property of Mathieu functions yields

$$\psi(\zeta_o, \eta_o) = \sum_{n=0}^{\infty} Ae_n \left\{Je_n(c_o, \zeta_o) - \frac{Je_n(c_o, 1)}{Ne_n(c_o, 1)} Ne_n(c_o, \zeta_o)\right\} \cdot Se_n(c_o, \eta_o)e^{-j\beta z}. \quad (13)$$

Employing the addition theorem of the Mathieu functions and applying the second boundary condition along with the orthogonal property of the triangular Mathieu functions, one can get a matrix equation similar to (10) with elements of the Z matrix given by

$$Z_{l,n} = Ke_{n,l}\left\{Je_l(c, \zeta_k) - \frac{Je_n(c_o, 1)}{Ne_n(c_o, 1)} Ne_l(c, \zeta_k)\right\}. \quad (14)$$

2) TM Odd Modes: Following the same procedure described for the TM even modes, but with $\psi(\zeta_o, \eta_o)$ represented in terms of odd functions [see (2)], one ends up with a matrix equation similar to that in (11), where the elements of the matrix are given by

$$Z_{l,n} = Ko_{n,l} Jo_l(c, \zeta_k) \quad (15)$$

and the coefficient vector is denoted as Ao_n.

III. Results and Discussion

To check the accuracy of our computations, the cutoff wavelengths of the confocal cases reported by Rozzi *et al.* [8] were recalculated using our method. Table I shows our results compared with those in [8]. As can be seen from Table I, there is excellent agreement. A maximum deviation of 1.8% in the results only occurs in a few cases.

For the general case, the effect of two parameters (strip width and cylinder focal length) on the cutoff wavelength was studied. First, the focal length of the elliptic cylinder was fixed, while the strip width is varied. Fig. 2(a) illustrates the change of the cutoff wavelength versus the strip width at some selected values of the focal length for the even TM case. As one can see from Fig. 2(a), the cutoff wavelength decreases when the strip width increases. On the other hand, one can see that, for the odd TE case, the cutoff wavelength increases with the strip width, as shown in Fig. 2(b). Second, the effect of the focal length on the cutoff wavelength at some selected values of strip width is illustrated in Fig. 3(a) for the even TM case, and in Fig. 3(b) for the odd TE case. In both cases, the cutoff wavelength decreases with an increase in the focal length of the elliptic cylinder, but the decrease in the even TM case is more rapid than in the odd TE case. Finally, values corresponding to the first three cutoff wavelengths for some selected parameters for both TM and TE cases are tabulated in Table II. It was found that, for the odd TM, cutoff wavelengths and even TE are independent of the strip width.

IV. Conclusion

The cutoff wavelengths for both TE and TM cases of an arbitrary strip width suspended in an elliptical cylinder have been calculated in this paper. It is found that the cutoff wavelength increases with the strip width for the odd TE case, while for all the other cases, it decreases.

Acknowledgment

The author wishes to thank the King Fahd University of Petroleum and Minerals, Dhahran, Saudi Arabia, for providing all the facilities required to perform this research.

References

[1] L. J. Chu, "Electromagnetic waves in elliptical pipes of metal," *J. Appl. Phys.*, vol. 9, pp. 583–591, Sept. 1938.

[2] J. G. Kretzschamar, "Wave propagation in Hollow conducting elliptical waveguides," *IEEE Trans. Microwave Theory Tech.*, vol. MTT-18, pp. 547–554, Sept. 1970.

[3] R. M. Bulley, "Analysis of the arbitrarily shaped waveguide by polynomial approximation," *IEEE Trans. Microwave Theory Tech.*, vol. MTT-18, pp. 1022–1028, Dec. 1970.

[4] B. K. Wang, K. Y. Lam, M. S. Leong, and P. S. Kool, "Elliptical waveguide analysis using improved polynomial approximation," *Proc. Inst. Elect. Eng.*, vol. 141, pp. 483–488, 1994.

[5] D. A. Goldberg, L. J. Jackson, and R. A. Rimmer, "Modes of elliptical waveguides: A correction," *IEEE Trans. Microwave Theory Tech.*, vol. 38, pp. 1603–1608, Nov. 1990.

[6] S. Zhang and Y. Shen, "Eigen-mode Sequence for an elliptical waveguide with arbitrary ellipticity," *IEEE Trans. Microwave Theory Tech.*, vol. 43, pp. 227–230, Jan. 1995.

[7] A. El-Sherbiny, "Cutoff wavelengths of ridged, circular, and elliptic guides," *IEEE Trans. Microwave Theory Tech.*, vol. MTT-21, pp. 7–12, Jan. 1973.

[8] T. Rozzi, L. Luca, and M. Ronzitti, "Analyzes of the suspended strip in elliptical cross section by separation of variables," *IEEE Trans. Microwave Theory Tech.*, vol. 45, pp. 1778–1784, Oct. 1997.

[9] J. A. Stratton, *Electromagnetic Theory*. New York: McGraw-Hill, 1941.

[10] K. Saermark, "A note on addition theorems for Mathieu functions," *Z. Angew. Math. Phys.*, vol. 10, pp. 426–428, 1958.

Scattering from Multiple Grooves in the Inner Conductor of a Coaxial Line

Hyo J. Eom, Young C. Noh, and Jong K. Park

***Abstract*—A problem of electromagnetic-wave scattering from multiple grooves in the inner conductor of a coaxial line is theoretically solved. Simultaneous equations for the discrete modal coefficients are formulated by utilizing the Fourier transform. The reflection and transmission coefficients are obtained in numerically efficient fast-convergent series. Numerical computations are performed to show the frequency characteristics of the reflection and transmission coefficients in terms of the groove geometry.**

***Index Terms*—Bandpass filter, coaxial line, Fourier transform, multiple grooves.**

I. Introduction

Electromagnetic-wave scattering from multiple grooves in the inner conductor of a coaxial line is of practical interest due to its frequency characteristics and the filter applications. A gap in the inner conductor was considered in [1]–[4], but a rigorous theoretical analysis for scattering from multiple grooves in a coaxial line seems to be little. In this paper, we intend to provide a rigorous theoretical analysis for scattering from multiple grooves in the inner conductor of a coaxial line by extending the Fourier transform technique, as used in [5]–[7]. In particular, we note that this paper is in continuation of [7], where scattering of a coaxial line terminated by a gap was considered. The rigorous solution presented in this paper is represented in a rapidly convergent series, which are simple and numerically efficient. The mathematical notations and analytical formulation closely follow those in [5]–[7].

II. Field Representation

Assume an incident TEM mode propagating from the left-hand side along a coaxial line whose inner conductor has N number of multiple grooves (see Fig. 1). In region I $(b < \rho < a)$, the H-field is a sum of the incident and scattered fields as

$$H^i_{\phi I}(\rho,\, z) = e^{ik_1 z}/(\eta_1 \rho) \tag{1}$$

$$H_{\phi I}(\rho,\, z) = \frac{i\omega\epsilon_1}{2\pi} \int_{-\infty}^{\infty} \frac{1}{\kappa}\, \tilde{E}(\zeta) R'(\kappa\rho) e^{-i\zeta z}\, d\zeta \tag{2}$$

where $\kappa = \sqrt{k_1^2 - \zeta^2}$, $\eta_1 = \sqrt{\mu_0/\epsilon_1}$, $R(\kappa\rho) = J_0(\kappa\rho)N_0(\kappa a) - N_0(\kappa\rho)J_0(\kappa a)$, $k_1 = \omega\sqrt{\mu_0\epsilon_1} = \omega\sqrt{\mu_0\epsilon_{r1}\epsilon_0}$, $R'(\kappa\rho) = (dR(\kappa\rho)/d(\kappa\rho))$, and $J_0(.)$ is the zeroth-order Bessel function and $N_0(.)$ is the zeroth-order Neumann function. Note that the scattered-field representation (2) accounts for the continuous TM-mode contribution in the spectral domain. In region II $(c < \rho < b)$ of permittivity ϵ_2

$$H_{\phi II}(\rho,\, z) = i\omega\epsilon_2 \sum_{n=1}^{N} \sum_{m=0}^{\infty} \frac{p_m^n}{\kappa_m^n} R_0'(\kappa_m^n \rho) \cos a_m^n \Big[z - s(n)\Big]$$

Manuscript received March 23, 1999.

H. J. Eom and J. K. Park are with the Department of Electrical Engineering, Korea Advanced Institute of Science and Technology, Taejon 305-701, Korea (e-mail: hjeom@ee.kaist.ac.kr).

Y. C. Noh is with the LG Information and Communications Ltd., Kyunggi-Do 431-080, Korea (e-mail: ycnoh@lgic.co.kr).

Publisher Item Identifier S 0018-9480(00)05474-0.

0018–9480/00$10.00 © 2000 IEEE

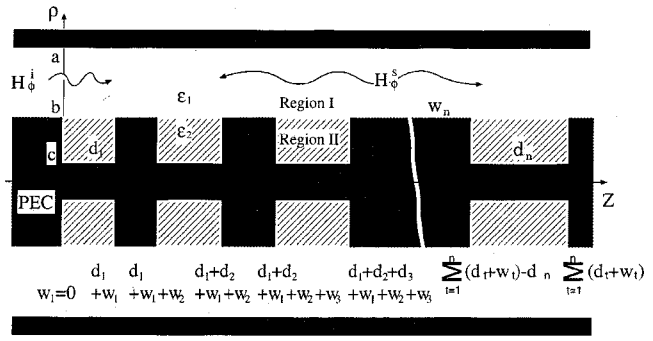

Fig. 1. Geometry of a coaxial line with multiple grooves in the inner conductor.

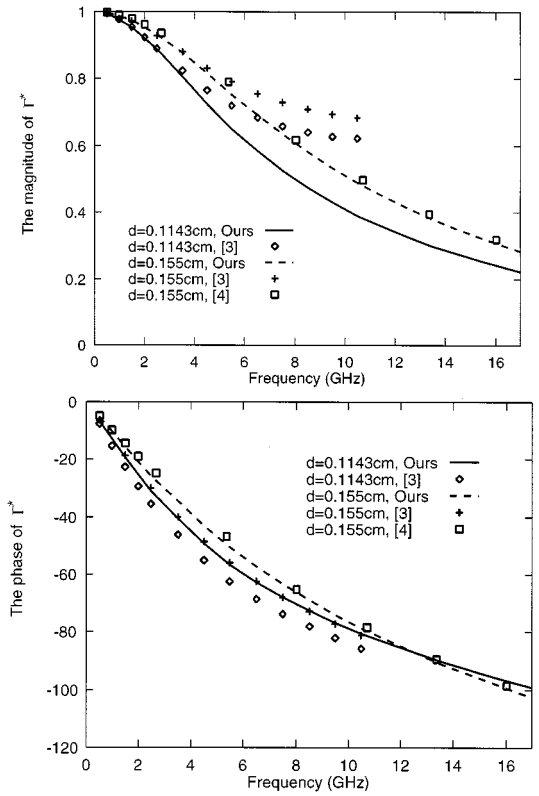

Fig. 2. Comparison of Γ for a single gap ($N = 1$, $c = 0$) in the inner conductor when $a = 0.714$ cm, $b = 0.310$ cm, $d_1 = d$, $\epsilon_{r1} = 1$, and $\epsilon_{r2} = 1$. Note that Γ^* is the conjugate of Γ and the result of $d = 0.1143$, [3] includes experimental data for 0.5∼2 GHz.

$$\times\left\{u\left[z-s(n)\right]-u\left[z-e(n)\right]\right\} \quad (3)$$

where

$$R_0(\kappa_m^n\rho)=\begin{cases}J_0(\kappa_m^n\rho)N_0(\kappa_m^n c)-N_0(\kappa_m^n\rho)J_0(\kappa_m^n c), \\ \quad \text{for } c\neq 0 \\ J_0(\kappa_m^n\rho), \qquad \text{for } c=0\end{cases} \quad (4)$$

$$s(n)=\sum_{t=1}^{n}(d_t+w_t)-d_n \quad (5)$$

$$e(n)=\sum_{t=1}^{n}(d_t+w_t) \quad (6)$$

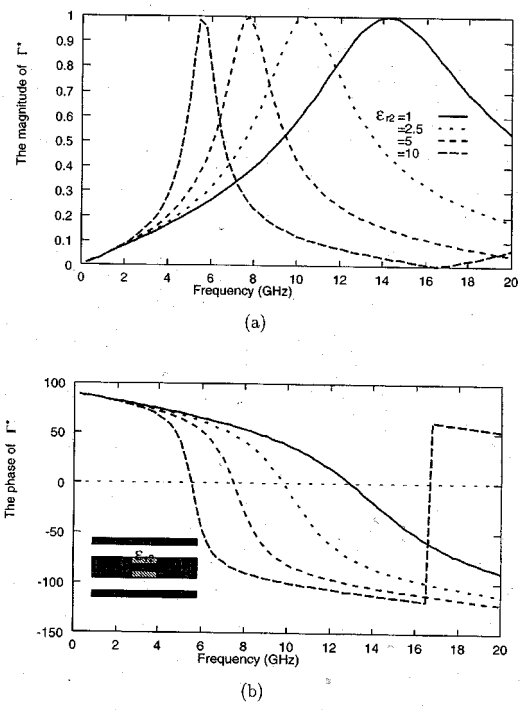

Fig. 3. Behavior of Γ^* for the different ϵ_{r2} for a single groove ($N = 1$, $c \neq 0$) in the inner conductor when $a = 0.714$ cm, $b = 0.310$ cm, $c = b/8$, $d_1 = 0.2a$, and $\epsilon_{r1} = 1$.

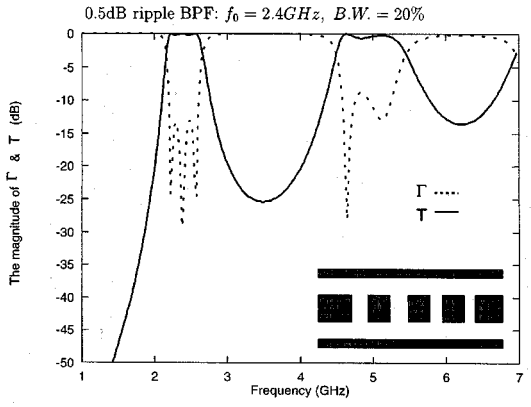

Fig. 4. Frequency characteristics of Γ and T for multiple gaps ($N = 4$, $c = 0$) in the inner conductor when $a = 0.714$ cm, $b = 0.310$ cm, $d_1 = 0.05$ cm, $d_2 = d_3 = 0.133$ cm, $d_4 = 0.05$ cm, $w_1 = 0$, $w_2 = 4.96$ cm, $w_3 = 5.32$ cm, $w_4 = 4.96$ cm, $\epsilon_{r1} = 1$, and $\epsilon_{r2} = 1$.

$\kappa_m^n = \sqrt{k_2^2-(a_m^n)^2}$, $k_2 = \omega\sqrt{\mu_0\epsilon_{r2}\epsilon_0}$, $a_m^n = m\pi/d_n$, $w_1 = 0$, $u(.)$ is a unit step function, N is the number of the grooves, and p_m^n is an unknown coefficient of the mode m in the nth groove. Note that d_t denotes the tth groove width and w_t denotes a distance between the $(t-1)$th and tth grooves. Applying the Fourier transform $\int_{-\infty}^{\infty}(\cdots)e^{i\zeta z}\,dz$ to the E_z boundary conditions at $\rho = b$

$$E_{zI}(b,\,z) = \begin{cases}E_{zII}(b,\,z), & \text{for } s(n)<z<e(n),\ n=1,\,2,\,3,\,\cdots,\,N \\ 0, & \text{for otherwise}\end{cases} \quad (7)$$

gives

$$\tilde{E}(\zeta) = \sum_{n=1}^{N} \sum_{m=0}^{\infty} \frac{p_m^n R_0(\kappa_m^n b)}{R(\kappa b)} G_m^n(\zeta) \tag{8}$$

where

$$G_m^n(\zeta) = \frac{-i\zeta\left[(-1)^m e^{i\zeta d_n} - 1\right]}{\zeta^2 - (a_m^n)^2} e^{i\zeta s(n)}. \tag{9}$$

The H_ϕ field continuity at $\rho = b$ over the groove gives

$$H_{\phi I}^i(b, z) + H_{\phi I}(b, z) = H_{\phi II}(b, z). \tag{10}$$

Multiplying (10) by $\cos a_l^p[z - s(p)]$ (where $l = 0, 1, 2, \cdots$ and $p = 1, 2, 3, \cdots, N$) and integrating with respect to z from $s(p)$ to $e(p)$, we obtain

$$\sum_{n=1}^{N} \sum_{m=0}^{\infty} \left\{ R_0(\kappa_m^n b) I_{ml}^{np} - \frac{d_n \epsilon_{r2} \alpha_m}{2\epsilon_{r1}\kappa_m^n} R_0'(\kappa_m^n b)\delta_{ml}\delta_{np} \right\} p_m^n = \frac{i}{k_1 b} G_l^p(k_1) \tag{11}$$

where $\alpha_m = 2(m = 0), 1(m = 1, 2, \cdots)$, δ_{ml} is the Kronecker delta and

$$I_{ml}^{np} = \frac{1}{2\pi} \int_{-\infty}^{\infty} \frac{R'(\kappa b)}{\kappa R(\kappa b)} G_m^n(\zeta) G_l^p(-\zeta)\, d\zeta. \tag{12}$$

Using the residue calculus, it is possible to transform (12) into rapidly converging series, which are efficient for numerical computation. From (11), we calculate the unknown coefficients p_m^n. After performing the residue calculus, we obtain the reflection coefficient Γ at $z = 0$ and the transmission coefficient T at $z = e(N)$ as

$$\Gamma = -\frac{H_{\phi I}}{H_{\phi I}^i} = -L_0^- \tag{13}$$

$$T = \frac{H_{\phi I}^i + H_{\phi I}}{H_{\phi I}^i} = 1 + L_0^+ \tag{14}$$

$$L_0^{\pm} = \mp \sum_{n=1}^{N} \sum_{m=0}^{\infty} \frac{p_m^n R_0(\kappa_m^n b) i k_1 \left[1 - (-1)^m e^{\mp i k_1 d_n}\right]}{2 \ln\left(\frac{b}{a}\right) (k_1^2 - (a_m^n)^2)} e^{\mp i k_1 s(n)}. \tag{15}$$

In a dominant-mode approximation ($k_1 d_1 \ll 1$) for a single groove ($N = 1$) in the inner conductor, (11)–(14) are simplified substantially with $m = 0$, thereby yielding

$$\Gamma = \frac{i\left[1 - e^{ik_1 d_1}\right]^2}{2bk_1^3 \ln(b/a) \left[I_{00}^{00} - \frac{\epsilon_{r2} d_1 R_0'(k_2 b)}{\epsilon_{r1} k_2 R_0(k_2 b)}\right]} \tag{16}$$

$$T = 1 + \frac{i\left[1 - e^{ik_1 d_1}\right]\left[1 - e^{-ik_1 d_1}\right]}{2bk_1^3 \ln(b/a) \left[I_{00}^{00} - \frac{\epsilon_{r2} d_1 R_0'(k_2 b)}{\epsilon_{r1} k_2 R_0(k_2 b)}\right]} \tag{17}$$

$$R_0(k_2 b) = \begin{cases} J_0(k_2 b) N_0(k_2 c) - N_0(k_2 b) J_0(k_2 c), & c \neq 0 \\ J_0(k_2 b), & c = 0. \end{cases} \tag{18}$$

III. Numerical Computations

Fig. 2 shows the comparison of Γ for a single gap ($N = 1$, $c = 0$) in the inner conductor between our and other results [3], [4] versus the frequency when $a = 0.714$ cm, $b = 0.31$ cm, $d_1 = d$, $\epsilon_{r1} = 1$, and $\epsilon_{r2} = 1$. Note that Γ^* is the conjugate of Γ. Our solution agrees well with the result of Sen and Saha [4]. In our computation, we use $m = 0$ in (11) to obtain p_m^n, indicating that our solution is numerically efficient. Our computational experience shows that a single mode ($m = 0$) solution satisfies the energy conservation to better than 0.1% error. Fig. 3 shows the behavior for a single groove ($N = 1$, $c \neq 0$) in the inner conductor versus ϵ_{r2} when $a = 0.714$ cm, $b = 0.31$ cm, $c = b/8$, $d_1 = 0.2a$, and $\epsilon_{r1} = 1$. As ϵ_{r2} increases from 1 to 10, the resonant frequency corresponding to $|\Gamma^*| \approx 1$ decreases. Fig. 4 illustrates the designed filter characteristics of reflection and transmission coefficients for four gaps ($N = 4$ and $c = 0$) in the inner conductor. The frequency characteristics in Fig. 4 are those of the 0.5-dB equal-ripple bandpass filter with the center frequency at 2.4 GHz and 20% bandwidth. When regions I and II are filled with a dielectric medium ($\epsilon_{r1} = \epsilon_{r2} = \epsilon_r > 1$), all physical dimensions ($a, b, d_1, \cdots, w_4$) of the designed filter should be accordingly normalized by $\sqrt{\epsilon_r}$. In other words, if $\epsilon_{r1} = \epsilon_{r2} = 2$, then $a = 0.714/\sqrt{2}$ cm, $b = 0.310/\sqrt{2}$ cm, ..., etc.

IV. Conclusion

In this paper, a rigorous solution for scattering from multiple grooves in the inner conductor of a coaxial line is obtained in closed form. Numerical computations are performed to illustrate the frequency characteristics for the reflection and transmission coefficients. Our theoretical results are useful for the filter design using the coaxial line with the multiple-grooved inner conductor.

References

[1] L. Young, "The practical realization of series capacitive coupling for microwave filters," *Microwave J.*, vol. 5, pp. 79–81, Dec. 1962.

[2] H. E. Green, "The numerical solution of some important transmission-line problem," *IEEE Trans. Microwave Theory Tech.*, vol. MTT-13, pp. 676–692, Sept. 1965.

[3] H. N. Dawirs, "Equivalent circuit of a series gap in the center conductor of a coaxial transmission line," *IEEE Trans. Microwave Theory Tech.*, vol. MTT-17, pp. 127–129, Feb. 1969.

[4] S. Sen and P. K. Saha, "Equivalent circuit of a gap in the central conductor of a coaxial line," *IEEE Trans. Microwave Theory Tech.*, vol. MTT-30, pp. 2026–2029, Nov. 1982.

[5] J. K. Park and H. J. Eom, "Fourier transform analysis of dielectric-filled edge-slot antenna," *Radio Sci.*, vol. 32, no. 6, pp. 2149–2154, Nov./Dec. 1997.

[6] J. K. Park and H. J. Eom, "Correction to Fourier transform analysis of dielectric-filled edge-slot antenna," *Radio Sci.*, vol. 33, no. 3, p. 631, May–June 1998.

[7] H. J. Eom, Y. C. Noh, and J. K. Park, "Scattering analysis of a coaxial line terminated by a gap," *IEEE Microwave Guided Wave Lett.*, vol. 8, pp. 218–219, June 1998.

Accurate Characterization of the Interaction Between Coupling Slots and Waveguide Bends in Waveguide Slot Arrays

Giuseppe Mazzarella and Giorgio Montisci

***Abstract*—In a waveguide slot array, it is sometimes required to introduce bent short-circuit terminations in the feeding network. This significantly affects the behavior of the coupling slots used in this network, with a very large variation in the coupling coefficient with respect to the standard case. A procedure to accurately evaluate the effect of such bends is presented, thus allowing to include them without any loss in the overall design accuracy. It is based on the method of moments, using a magnetic-field integral equation expressed in terms of the vector potential, which appears to be the most efficient way for waveguide problems. The development is aimed at a very effective implementation, which allows to include it in design tools for waveguide slot arrays without increasing the total computational load, and has been assessed through comparison with experimental results.**

***Index Terms*—Slot array, slot coupler.**

I. Introduction

Through their use dates back to the 1940's, slot arrays are still quite popular as high-performance antennas, mainly in the higher part of the microwave band. Such antennas guarantee a very high efficiency, usually a very low crosspolar level and a compact realization. Moreover, their design can be done with a great accuracy.

The basic array (or sub-array) structure consists of a main waveguide which feeds, through a rotated slot [1], a number of crossed branch waveguides containing the radiating slots. The coupling slot is a series one, thus, the feeding guide must be terminated with a short-circuit a half-wavelength beyond the center of the last coupling slot and, therefore, juts out of the radiating waveguides [see Fig. 1(a)]. This causes an enlargement of the array that cannot be always tolerated. Moreover, when a slot array is used as a monopulse radar antenna, with the four quadrants separately fed, there is absolutely no room to accommodate this long short-circuit section. In all these cases, the best solution is to bend the waveguide end with a 90° or a 180° curve, as in the transverse section of Fig. 1(b) and (d) (see also Fig. 1(c) for a three-dimensional (3-D) view of the single-bent short-circuit termination). Both an *isolated* waveguide bend [2] and an *isolated* coupling slot [3] can be analyzed by known techniques, but those techniques cannot be used in our case since the slot is not isolated, except inside the curved section. Therefore, it interacts with the bend through its *near field*. In this paper, we describe an accurate modeling technique for such a *near-field* interaction, fully taking into account also the waveguide wall thickness. This is obtained with a full-wave method of moment (MoM) procedure. A set of coupled integral equations are obtained by forcing the continuity of the tangential magnetic field at both slot apertures and at the input section of each bent waveguide stub [see Fig. 1(b) and (d)]. The magnetic field in the waveguide is expressed through the Fitzgerald vector potential $\boldsymbol{F}$ computed using its Green function expressed as modal series. Discretization of the unknown magnetic currents and the Galerkin procedure then lead to a linear system whose solutions give the magnetic currents and the scattering matrix of the junction.

Manuscript received April 27, 1999. This work was supported by the Alenia Difesa—Unità Officine Galileo.

The authors are with the Dipartimento Ingegneria Elettrica ed Elettronica, Università di Cagliari, 09123 Cagliari, Italy (e-mail: mazzarella@diee.unica.it).

Publisher Item Identifier S 0018-9480(00)05477-6.

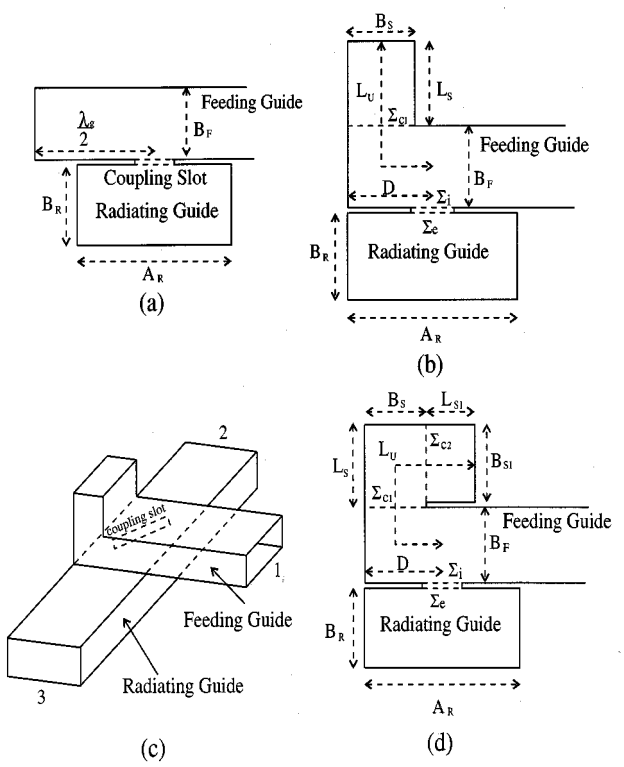

Fig. 1. (a) Geometry of the coupling slot and standard short-circuit termination λ_g is the feeding guide TE_{10} wavelength. (b) Transverse section of the coupling slot and of the single-bent short-circuit termination. (c) Perspective view of the coupling slot and of the single-bent short-circuit termination. (d) Transverse section of the coupling slot and of the double-bent short-circuit termination.

This strategy is surely able to get a very accurate analysis of the coupler, but its use must be carefully assessed in an array design procedure. As a matter of fact, array design procedures usually require a very large number of slot analysis and, therefore, the computational weight of a full-wave approach can be too large to prevent its use. Therefore, an analysis procedure that must be both accurate and effective for use in array design, is needed to overcome this problem. To this end, the strategy proposed here have been developed into an analysis procedure in which all steps have been carefully devised and implemented to reach the goal of a very effective and accurate characterization of a slot in a bent termination. First, an entire domain basis function representation for the unknown currents has been used. As discussed, e.g., in [4], this requires a very small number of unknowns. The resulting linear system is, therefore, small and can also be well conditioned. Moreover, the matrix elements, which are no more than field–current reactions computed over surfaces whose size is comparable with the wavelength, varies very smoothly with the frequency or the geometrical parameters. This suggests that a polynomial interpolation of the matrix elements [5] will significantly reduce the matrix fill time by more than an order of magnitude, and the same reduction is obtained in the total analysis time since the system solution requires a very small fraction of the total computational time. The interpolation error involved is negligible even for three-point Lagrange interpolation used here (for details, see [6]).

II. Problem Formulation

According to the equivalence theorem, all apertures in the structures shown in Fig. 1(b) and (d) can be replaced by the suitable equivalent

0018–9480/00$10.00 © 2000 IEEE

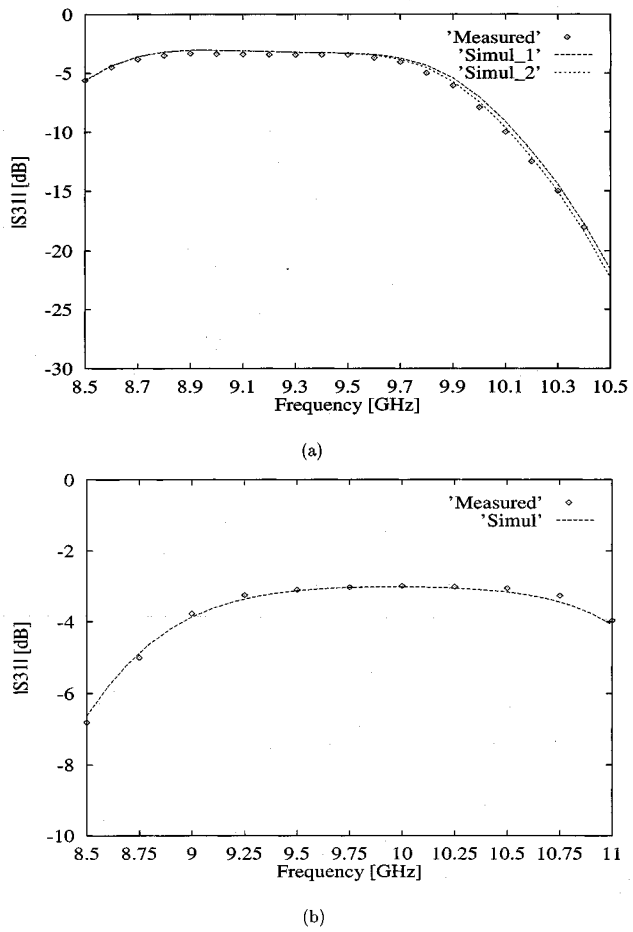

Fig. 2. Modulus of the coupling coefficient S_{31} between: (a) two WR90 guides ($A = 22.86$ mm, $B = 10.16$ mm), $B_S = B_F$, $L_S = 12.80$ mm (measured: experimental data, Simul-1: $\mathcal{K} = 96.2$ cm^{-1}, three expansion functions on the slot, 24 modes on Σ_{c1}, Simul-2: $\mathcal{K} = 41.2$ cm^{-1}, five expansion functions on the slot, 60 modes on Σ_{c1}), (b) two half-height WR90 guides ($A = 22.86$ mm, $B = 5.08$ mm), $B_S = B_{S1} = B_F$, $L_S = 6.35$ mm, $L_{S1} = 6.1$ mm (measured: experimental data, Simul: $\mathcal{K} = 41.2$ cm^{-1}, three expansion functions on the slot, 24 modes on Σ_{c1}, and Σ_{c2}). In both cases, $\theta = 33^\circ$, slot length $= 15.6$ mm, slot width $= 3.0$ mm, waveguide wall thickness $= 1.0$ mm, and $D = A_R/2$.

magnetic current $\boldsymbol{M_i}$ on Σ_i, $\boldsymbol{M_e}$ on Σ_e, and $\boldsymbol{M_{ci}}$ on Σ_{ci}. These currents are unknowns and can be computed by enforcing the continuity of the tangential magnetic field at the apertures themselves. As a matter of fact, taking the wall thickness into account requires to use an equivalence theorem on both slot apertures and, therefore, two different unknowns and equations are needed. Including an incident TE_{10} in the *radiating* guide field as forcing term, we get a set of magnetic-field integral equations (MFIE's) whose solution allows to compute all entries of the scattering matrix. There is a continuity equation for each aperture (Σ_e, Σ_i, Σ_{c1}, etc.). For the 90° bend, these equations are

$$\begin{aligned} \boldsymbol{H_S} &= \boldsymbol{H_{RG}} + \boldsymbol{H_{inc}}, \qquad \text{on } \Sigma_e \\ \boldsymbol{H_{FG}} &= \boldsymbol{H_S}, \qquad \text{on } \Sigma_i \\ \boldsymbol{H_B} &= \boldsymbol{H_{FG}}, \qquad \text{on } \Sigma_{c1} \end{aligned} \tag{1}$$

where

- $\boldsymbol{H_{inc}}$ Incident TE_{10}.
- $\boldsymbol{H_{FG}}$ Magnetic field in the feeding guide region, which depends on $\boldsymbol{M_i}$ and $\boldsymbol{M_{c1}}$.
- $\boldsymbol{H_S}$ Magnetic field in the slot region, which depends on $\boldsymbol{M_i}$ and $\boldsymbol{M_e}$;
- $\boldsymbol{H_{RG}}$ Magnetic field in the radiating guide region, which depends on $\boldsymbol{M_e}$.
- $\boldsymbol{H_B}$ Magnetic field in the waveguide bend region, which depends on $\boldsymbol{M_{c1}}$.

For the 180° bend, a further equation on Σ_{c2} is required. Since $\boldsymbol{H_{FG}}$, $\boldsymbol{H_S}$, $\boldsymbol{H_{RG}}$, and $\boldsymbol{H_B}$ depend upon the unknown currents, (1) can be seen as a set of integral equations, which can be transformed by the MoM into a set of linear algebraic ones.

All unknown currents are expressed as a linear combination of suitable basis functions. The slot is usually narrow enough to neglect the longitudinal component of the electric field on it [3]. Therefore, only the axial-directed magnetic current is used as an unknown.

Since all computational surfaces have a rectangular shape, entire domain basis functions have been used everywhere. The slot currents are expressed as truncated Fourier series with respect to the axial coordinate ξ (centered on the slot), as

$$\boldsymbol{M} = \sum_{p=1}^{N} a_p \sin\left[\frac{p\pi}{L}(\xi + \frac{L}{2})\right] \boldsymbol{i}_\xi = \sum_{p=1}^{N} a_p \boldsymbol{f}_p(\xi) \tag{2}$$

wherein a_p are the expansion coefficients, which are different on the internal and external surfaces of the slot, $\boldsymbol{f}_p$ are the expansion functions, and L is the slot length. The bent termination can be considered as a "stub" waveguide. The magnetic current upon its aperture section Σ_{c1} is discretized in a way similar to (2), but using as basis functions the currents corresponding to the well-known [7] tangential electric field of the stub waveguide modes. The section Σ_{c2}, if present, is dealt with in the same way.

To compute the unknown currents, (2) is substituted into (1) and the resulting MFIE equations are scalar multiplied by the test functions and integrated over the corresponding aperture Σ to get a linear system in the unknown coefficients. Since the basis functions form a complete set on each aperture, they are also the best choice for test functions (Galerkin procedure) because the resulting linear equations are the most accurate approximation, in the mean square norm, of the integral equations for a given number of test functions. A few terms in (2) are needed to compute the response over a quite wide frequency range around the resonant frequency of the slot so that the resulting linear system is small. Moreover, since we have chosen orthogonal basis functions, the system is also quite well conditioned.

Now the $\boldsymbol{H}$-field Green function has a Dirac delta singularity at the source location [7], whatever the magnetic current direction, while its modal series expansion contains only an axial impulsive term. The other singular components are *hidden* into the modal series and this causes a poorer convergence of the series and, in some cases, even a divergent behavior. As a consequence, the MoM matrix elements computation is quite difficult, whatever method is used. To simplify the computation, the waveguide magnetic field can be expressed through the vector potential $\boldsymbol{F}$, which has only a mild singularity at the source location.

Since $\boldsymbol{H} = j\omega\varepsilon\boldsymbol{F} + 1/(j\omega\mu)\nabla\nabla\cdot\boldsymbol{F}$, wherein ω is the angular frequency and ε, μ are the permittivity and permeability of the medium in which $\boldsymbol{H}$ is computed, we need both the $\boldsymbol{F}$ potential and its divergence. In a waveguide, these can be computed in terms of the magnetic current $\boldsymbol{M}$ as a modal series (see [8]), in the same way as the H-field Green function can [7]. Use of those Green functions for $\boldsymbol{F}$ and $\nabla\cdot\boldsymbol{F}$, therefore, lead to a modal series representation for the matrix term. These series are truncated, retaining all modes whose cutoff wavenumber is smaller than a given value $\mathcal{K}$.

III. Experimental Assessment and Results

In order to assess the procedure described in the previous sections, we have compared for both structures in Fig. 1(b) and (d) the results of

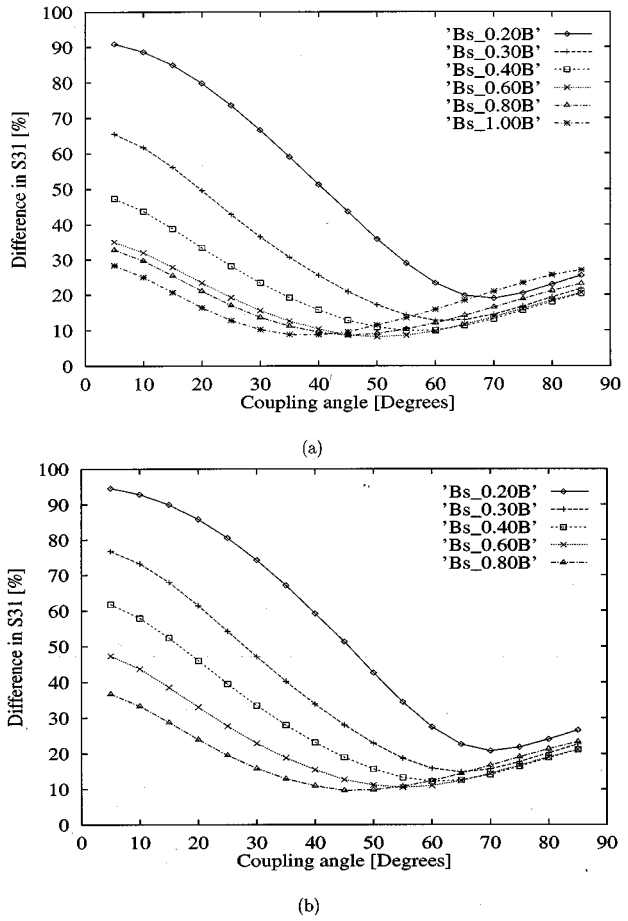

Fig. 3. Difference in S_{31} between a coupler with a standard short circuit and a coupler with: (a) a single-bent or a (b) double-bent short circuit for $B_S(= B_{S1}$ varying from $0.2B$ and B. Frequency $= 28.4$ GHz, slot length $= 5.112$ mm, slot width $= 0.625$ mm, waveguide wall thickness $= 1.016$ mm, and $D = A_R/2$, $L_U = \lambda_g/2$.

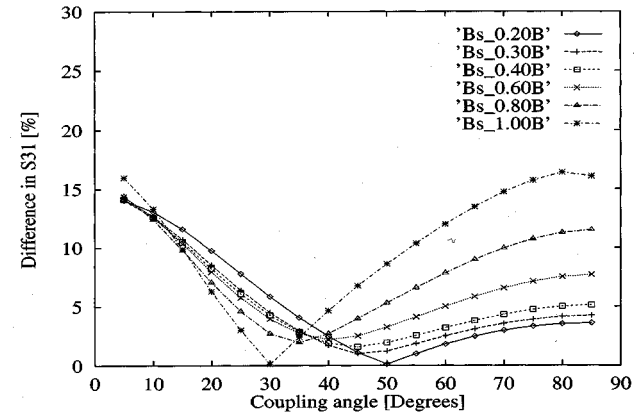

Fig. 4. Variation in S_{31} with respect to the values for a slot isolated from the termination. All data as in Fig. 3(a).

our simulations with some experimental data. Of course, the accuracy of our procedure depends on the number of expansion functions on each section and on the truncation level of the modal series. In Fig. 2(a), two different configurations of these parameters are considered. From it can be observed that $\mathcal{K} = 41.2$ cm $^{-1}$, three expansion functions on the slot, and 24 modes on Σ_{c1} are enough to get an accurate response. These values will, therefore, be used for all subsequent results. Larger values are required only for highly accurate design. It is worth noting that such a few expansion terms are needed not only at the resonance, as claimed in [3], but over all the wide frequency range considered here.

The experimental comparison presented in Fig. 2(a) (coupler with a single-bent short-circuit termination) and in Fig. 2(b) (coupler with a double-bent short-circuit termination) shows that our procedure is indeed able to deal accurately with the *near-field* interaction between the slot and bend. Of course, it is also important to quantitatively evaluate the impact of that near-field interaction. The best way to do this is to consider the coupling coefficient S_{31} between the feeding and radiating guides and to evaluate its percentage variation due to the bend with respect to a straight short circuit spaced $\lambda_g/2$ from the coupling slot [6]. To get a meaningful comparison, the *unfolded* length L_U of the bent short circuit must be the same as the length of the standard short circuit, i.e., $\lambda_g/2$ in our case, and this requires a rule to unfold the termination. A reasonable assumption, supported by our test, is that the unfolded length must be evaluated along the center line of the waveguides. This leads, for the unfolded length, to $L_U = L_S + B_F/2 + D - B_S/2$ and $L_U = L_{S1} + L_S + B_F/2 + D - B_{S1}/2$, respectively, for the 90° and 180° bends [the symbols are defined in Fig. 1(b) and (d)]. Any other value for L_U causes a larger difference with respect to the standard short-circuit termination.

A typical case is shown in Fig. 3(a) for a single bend and in Fig. 3(b) for a double bend. There, a coupling slot between two WR28 guides ($A = 7.112$ mm, $B = 3.556$ mm), rotated to from an angle θ with respect to the feeding waveguide axis, is considered. The slot length allows the slot to resonate at the chosen test frequency (28.4 GHz) for a tilt angle $\theta = 45^\circ$. Since the resonant length of the isolated slot does not vary very much with the tilt angle for our standard guides [3], we decided to use the same slot length for all the cases shown.

From the results shown in Fig. 3, it appears that the difference in the coupling coefficient is significant. Of course, this difference is partly due to the near-field interaction and partly to the bend itself. In order to evaluate only the near-field interaction effect, we have computed the variation of the coupling coefficient with respect to the case when slot and termination are independent [6]. The difference, for the same case as Fig. 3(a), is shown in Fig. 4. It appears that this difference can be as high as 15% and the near-field interaction, therefore, cannot be neglected. The double-bent termination [as in the case of Fig. 3(b)] gives almost exactly the same curves.

IV. Conclusion

A full wave MoM procedure to take into account the near-field interaction between a series slot and a bent waveguide short-circuit has been described, which allows to use such bends in waveguide slot arrays without any loss in the design accuracy.

All the procedure steps have been carefully devised to get a very good accuracy and, at the same time, a very effective implementation. This allows its use in array design procedure. It is also worth noting that the same *near-field* interaction between an aperture and a 90° waveguide curve analyzed here also appears or can be used in other microwave devices. For instance, a more compact waveguide directional coupler can be realized using 90° curves centered at the first and last coupling holes location instead of the standard rounded curves. To analyze such a device, the *near-field* interaction must be taken into account.

References

[1] R. S. Elliott, *Antenna Theory and Design*. Englewood Cliffs, NJ: Prentice-Hall, 1981.
[2] N. Marcuvitz, *Waveguide Handbook*. New York: McGraw-Hill, 1951.

[3] S. R. Rengarajan, "Analysis of a centered-inclined waveguide slot coupler," *IEEE Trans. Microwave Theory Tech.*, vol. 37, pp. 884–889, May 1989.
[4] G. S. Stern and R. S. Elliott, "Resonant length of longitudinal slots and validity of circuit representation: Theory and experiments," *IEEE Trans. Antennas Propagat.*, vol. AP-33, pp. 1264–1271, Nov. 1985.
[5] K. L. Virga and Y. Rahmat-Samii, "Efficient wide-band evaluation of mobile communications antennas using $[Z]$ or $[Y]$ matrix interpolation with the method of moments," *IEEE Trans. Antennas Propagat.*, vol. 47, pp. 65–76, Jan. 1999.
[6] G. Mazzarella and G. Montisci, "Full-wave analysis of waveguide slot couplers using a mixed potential formulation," *Alta Freq.*, vol. 11, pp. 20–24, 1999.
[7] R. E. Collin, *Field Theory of Guided Waves*, 2nd ed. Piscataway, NJ: IEEE Press, 1991.
[8] G. Mazzarella and G. Montisci, "A rigorous analysis of dielectric-covered narrow longitudinal shunt slots with finite wall thickness," *Electromag.*, vol. 19, pp. 407–418, 1999.

A Varactor-Tuned RF Filter

Andrew R. Brown and Gabriel M. Rebeiz

***Abstract*—An electronically tunable filter at 1 GHz is presented in this paper. The filter uses a suspended substrate design and commercially available varactors for filter tuning. The filter has a 60% tuning range from 700 MHz to 1.33 GHz with a low insertion loss (better than 3 dB from 1 to 1.33 GHz). This paper discusses the effects of the varactor series resistance and the electrical length of the distributed resonator on the overall resonator quality factor and filter insertion loss. The input third-order intermodulation product intercept point was measured to be better than 17 dBm across the entire tuning range.**

***Index Terms*—Frequency control, tunable filters.**

I. Introduction

Low-loss tunable frequency filters are often used as tracking filters for multiband telecommunication systems, radiometers, and wide-band radar systems. Typically, tracking filters are mechanically tuned by adjusting the cavity dimensions of the resonators or magnetically altering the resonant frequency of a ferromagnetic YIG element [1], [2]. Neither of these approaches can easily by miniaturized or produced in large volumes for wireless communication products. The filters must be custom machined, carefully assembled, tuned, and calibrated. An alternative to the mechanically tuned and YIG filters is based on solid-state varactor diodes. Varactor filters have previously been developed using two– to three-pole filters [3]–[5]. However, the effects of the varactor series resistance and electrical length of the distributed portion of the resonator have not been investigated.

An electrically tunable capacitively loaded interdigital filter is presented in this paper. The tuning element is a reverse-biased varactor diode. The resonators of the tunable filter are shortened interdigital fingers with varactor diodes at the ends. The coupling is carefully controlled by the geometry of the fingers and the tuning is performed by changing the bias on the varactor diodes. Since both the interdigital fingers and diodes are carefully controlled and fabricated in batch, this filter can be easily produced in large quantities. The varactor-controlled tunable filter is based on a suspended substrate stripline technology. The suspended substrate allows for a very low effective dielectric constant, resulting in very wide low-loss transmission lines.

Manuscript received April 29, 1999. This work was supported by Army Research Office under Contract DAAH04-95-1-0205 and Contract DAAG55-98-1-0227.

The authors are with the Radiation Laboratory, Department of Electrical Engineering, The University of Michigan at Ann Arbor, Ann Arbor, MI 48109 USA (e-mail: mscout@engin.umich.edu; rebeiz@engin.umich.edu).

Publisher Item Identifier S 0018-9480(00)05473-9.

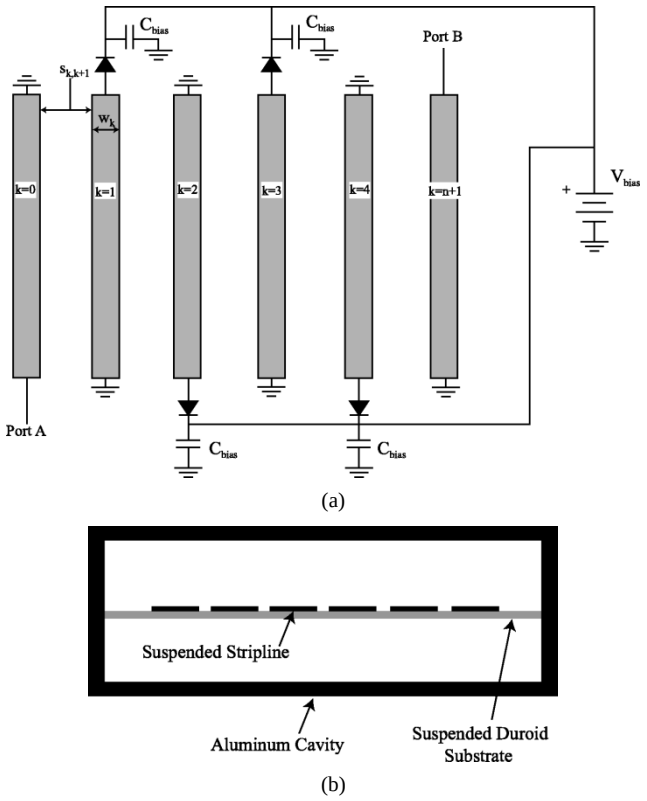

Fig. 1. (a) Topology of the varactor loaded interdigital bandpass filter. (b) Cross section of suspended substrate stripline.

II. Center Frequency of a Varactor-Loaded Transmission-Line Resonator

The design of a varactor-loaded interdigital filter is similar to the capacitively loaded combline filter presented in [1], but is adapted for the interdigital topology. The interdigital filter is a symmetric filter of coupled resonators. The first finger at the input and output ports is a shorted line that acts as an impedance transformer for the filter. This is the only line with a fixed termination. The interior coupled lines are shorted at one end and loaded with varactor diodes at the other end (Fig. 1). To allow for biasing, large capacitors are added ($C_{\rm bias}$). When the bias voltage is changed, the thickness of the depletion region of the varactor diodes changes. This alters the capacitance of the varactor tuning the resonant length of fingers. The width and separation of the interior lines are determined only by the bandwidth of the normalized filter response function, and is independent of the center frequency. The center frequency of the filter is determined by the resonant lengths of the lines, which is tuned by the varactors. The tuning range for the filter is limited by the fixed lengths of the input and output finger lengths, internal impedance of the filter, range of capacitance of the varactor diodes, and electrical length of the fingers.

The electrical length of a single finger θ without the capacitive loading is given by

$$\theta(V_{\rm bias}) = 2\pi f l \sqrt{\epsilon_{\rm eff}}/c \tag{1}$$

0018–9480/00$10.00 © 2000 IEEE

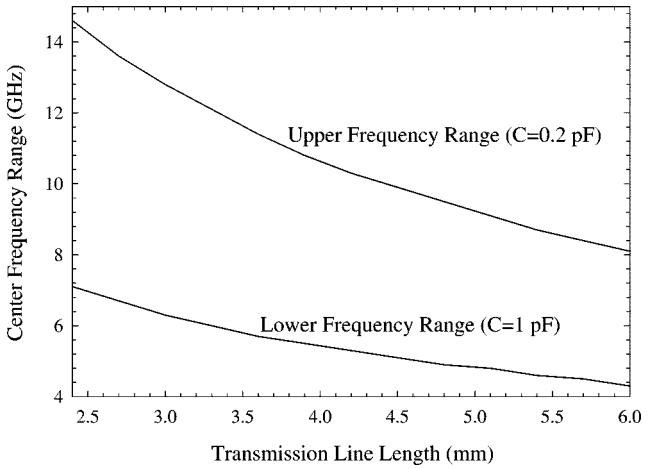

Fig. 2. Theoretical resonant frequency tuning range for a varactor with a capacitance range of 0.2–1.0 pF as a function of transmission-line physical length.

where f is the frequency, l is the length of the fingers, ϵ_{eff} is the effective relative dielectric constant (approximately 1.05 for membrane supported microstrip), and c is the speed of light. If the finger is loaded by a shunt capacitance, the effective length of the transmission line increases. If the amount of capacitance added increases the overall effective length to $\pi/2$, and the transmission line is shorted at one end, as in the case of the interdigital filter, then the capacitively loaded transmission line behaves as a quarter-wave resonator. In order to achieve resonance, the reactance of the transmission line and varactor must cancel ($X_{\text{Varactor}} + X_{T-\text{Line}} = 0$). By using a lossless transmission-line approximation ($X_{T-\text{Line}} = Z_{ak} \tan\theta$ where Z_{ak} is the intrinsic impedance of the kth finger), the necessary capacitance is given by

$$C_{\text{var}} = \frac{1}{Z_{ak} 2\pi f_0 \tan\theta_0} \tag{2}$$

where f_0 and θ_0 are the frequency and electrical length of the finger at resonance. Conversely, the resonant frequency of the varactor-loaded finger for a given capacitance is

$$f_0(V_{\text{bias}}) \approx \frac{1}{Z_{\text{ak}} 2\pi C_{\text{var}}(V_{\text{bias}}) \tan\left(\theta_0(V_{\text{bias}})\right)} \tag{3}$$

where f_0, C_{var}, and θ_0 are now functions of the bias voltage. Note that this is a transcendental.

From (3), a larger tuning range is obtained by making Z_{ak} small. An internal impedance of 60 Ω was chosen. This is a relatively low impedance line while still maintaining a reasonable conductor width for loss considerations.

The resonant frequency [see (3)] was solved graphically for the upper and lower tuned center frequencies as a function of physical length of the transmission lines assuming a varactor with a capacitance range of 0.2–1.0 pF (Fig. 2). This is a typical varactor value for an X-band tunable filter. This can be scaled in frequency by the transmission-line physical length and the capacitance value. According to Fig. 2, the length of the transmission-line segment should be as short as possible for the widest tuning range. However, the series resistance of the varactor has a stronger influence on the quality factor of the resonators, as the transmission-line section decreases where the quality factor is taken as the combination of the transmission-line segment and varactor.

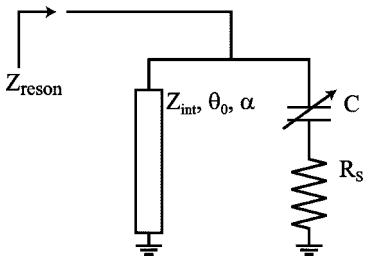

Fig. 3. Model of a varactor-loaded transmission-line resonator.

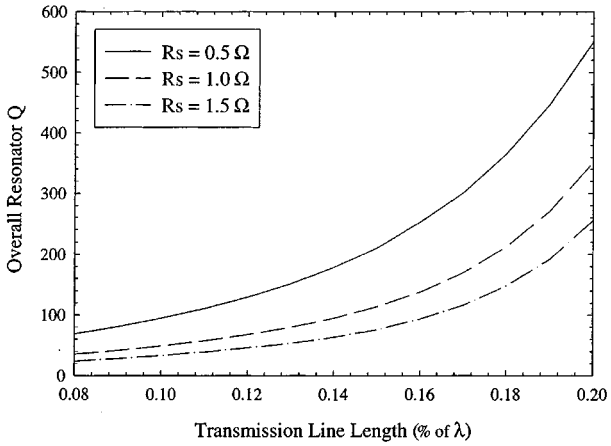

Fig. 4. Overall resonator quality factor as a function of transmission-line length for a transmission-line quality factor of 1030.

TABLE I
RF TUNABLE FILTER FINGER DIMENSIONS

Finger, k	w_k	$g_{k-1,k}$
0	9.63 mm	
1	5.97 mm	0.25 mm
2	7.11 mm	2.87 mm
3	7.11 mm	3.51 mm
4	5.97 mm	2.87 mm
5	9.63 mm	0.25 mm

III. QUALITY FACTOR OF A VARACTOR-LOADED TRANSMISSION LINE

The quality factor of the resonant fingers is a function of the intrinsic impedance, line length, attenuation of the line, and series resistance of the varactor. The resonator can be viewed as a short transmission line in parallel with a varactor to ground, as in Fig. 3, where R_s is the series resistance of the varactor and α is the loss of the transmission line. It is necessary to define two different definitions for the quality factor; namely, the transmission-line quality factor and the overall resonator quality factor. The transmission-line quality factor is the unloaded Q of the transmission line without the varactor loading. The overall resonator quality factor is the unloaded Q of the transmission line with the varactor loading. The input impedance of the shorted transmission line alone is

$$Z_{\text{line}} = Z_{int} \frac{\tanh(\alpha l) + j \tan(\beta l)}{1 + j \tan(\beta l) \tanh(\alpha l)}. \tag{4}$$

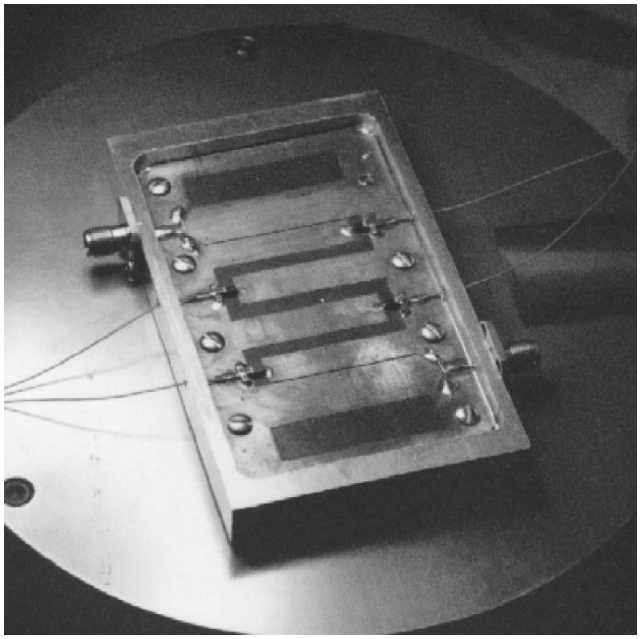

Fig. 5. RF varactor tuned bandpass filter.

The input impedance of the varactor alone including the series resistance is

$$Z_{\text{cap}} = \frac{1}{j\omega C} + R_s \tag{5}$$

$$= -j\frac{\omega_0}{\omega} Z_{\text{int}} \tan\theta + R_s. \tag{6}$$

The total impedance can be found by taking the parallel combination. The 3-dB bandwidth can be determined by finding the bandwidth where the magnitude of the impedance falls by a factor of $\sqrt{2}$ giving the reciprocal of the overall resonator unloaded quality factor. As the filter tunes, the electrical length of the transmission line changes altering the overall resonator quality factor. Fig. 4 shows the resulting overall resonator quality factor as a function of resonator electrical length and diode series resistance. As the transmission line becomes electrically short, the transmission-line quality factor has a decreasing effect. For wavelengths where the line is less than 0.1λ, the transmission-line quality factor is not very significant, and the varactor series resistance controls the overall resonator quality factor. As the transmission-line portion becomes electrically longer, the overall resonator quality factor is strongly dependent on the transmission-line quality factor, showing the advantages of the suspended substrate transmission lines. However, this comes at the expense of the tuning range. Based on (3), the tuning range for a given capacitance ratio decreases considerably with increasing electrical length.

IV. RF Tunable Filter

The RF tunable filter was fabricated on 127-μm RT/Duroid[1] with a dielectric constant of 2.2. The circuit was suspended over an aluminum cavity. The depth of the cavity was 4 mm with an attached 4-mm top shielding cover. The finger length is 0.13λ at 1.25 GHz (3.1 cm) with an internal impedance of 60 Ω and a filter bandwidth of 16% with a ripple of 0.2 dB. The linewidths and gaps are summarized in the Table I where w_k is the width of the kth filter finger and $g_{k-1,\,k}$ is the gap between fingers $k-1$ and k. The transmission-line quality factor for this structure is 1030 at 1.25 GHz.

[1]Rogers Corporation, Rogers, CT.

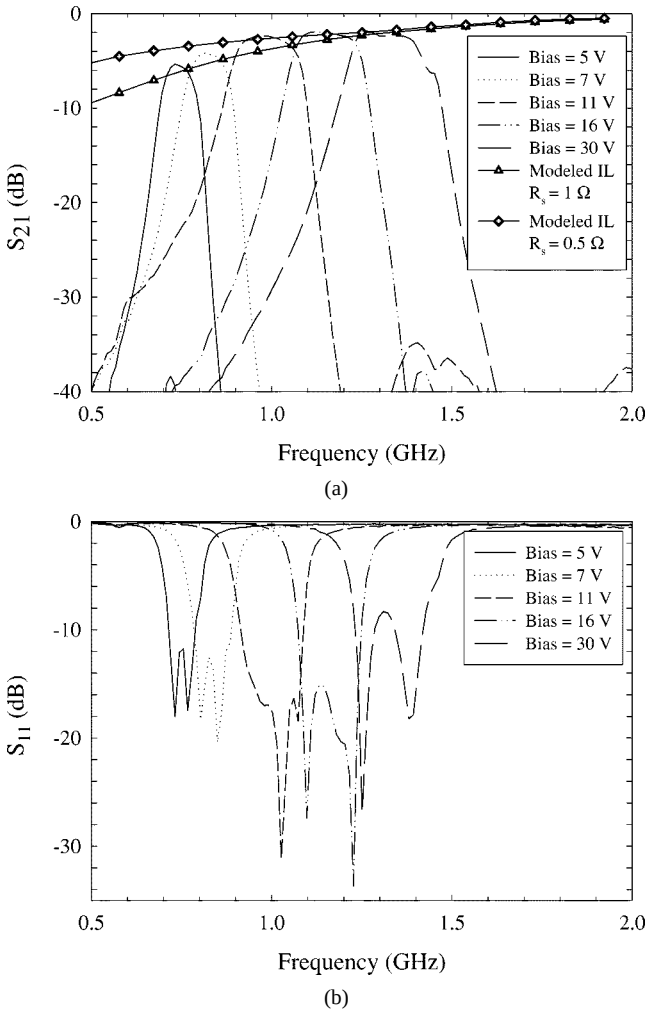

Fig. 6. RF tunable filter, (a) measured insertion loss, and (b) return loss for various bias levels.

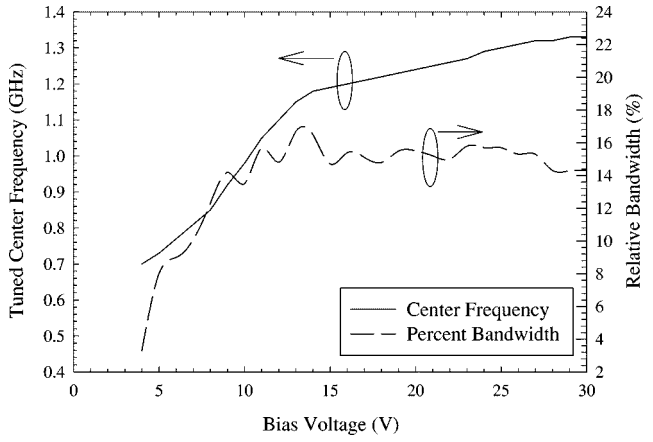

Fig. 7. Measured center frequency and relative bandwidth as a function of bias voltage.

The varactors are BB811 RF Variable Capacitance Diodes[2] with a series resistance of about 1 Ω and a junction capacitance from 1 to 8.8 pF over a 30-V bias range.[3] The varactors are biased equally with a 75-pF capacitor from the bias line to ground to provide an RF short for

[2]Phillips Semiconductor, Sunnyville, CA.

[3]Device parameters based on manufacturer supplied data.

TABLE II
INTERMODULATION MEASUREMENTS

Bias	f_0	Input IP3
5 V	720 MHz	24.0 dBm
7.5 V	830 MHz	28.1 dBm
10 V	970 MHz	17.9 dBm
15 V	1130 MHz	18.5 dBm
20 V	1220 MHz	23.0 dBm

the varactor and an open circuit for the bias (see Fig. 1). The predicted tuning range is from 660 MHz to 1.6 GHz (83% tuning range) with all varactors biased equally in parallel (Fig. 5).

The measured response of the filter showed a 60% tuning bandwidth from 700 MHz to 1.33 GHz (Fig. 6). The measured center frequency and bandwidth as a function of varactor bias voltage are shown in Fig. 7. The filter input matching is good with a return loss of better than -10 dB over the tuning range up to 1.3 GHz. At center frequencies below 1 GHz, the bandwidth is reduced and the insertion loss increases. The reduced bandwidth is due to the bandwidth of the impedance inverter network of coupled lines at the input and output of the filter. The increase in insertion loss at the low end of the tuning range is due to the decrease in overall resonator quality factor as the electrical length of the transmission-line portion becomes shorter.

The theoretical insertion loss, assuming a 16% bandwidth 0.2-dB-ripple Chebyshev four-pole filter, was calculated based on the modeled overall resonator quality factor with a varactor series resistance of 0.5 and 1 Ω from Fig. 4, and is plotted in Fig. 6(a). There is a good agreement with measured and calculated insertion loss. For center frequencies above 1 GHz, the insertion loss is less than 3 dB in the passband. The series resistance of the varactor diode is the major limiting factor in the filter insertion loss. Still, the tuned RF filter performance is comparable to state-of-the-art YIG and mechanically tuned filters at only a fraction of the material and assembly cost.

Finally, the filter was measured under large-signal tests. With a single large-signal tone, the input power was increased to 20 dBm without reaching a 1-dB compression point.

The third-order intermodulation intercept point was measured under different bias conditions. In all cases, both signals and their associated third-order mixing products were within the passband of the filter (two fundamentals separated by 2 MHz). This is a worst-case situation in that the filter has no effect on attenuating mixing products due to the nonlinearities of the varactors. The results of this are shown in Table II. In all cases, the input third-order intermodulation product intercept point (IIP3) was better than 17 dBm.

REFERENCES

[1] G. L. Matthaei, L. Young, and E. M. T. Jones, *Microwave Filters, Impedance-Matching Networks, and Coupling Structures*. Norwood, MA: Artech House, 1980.

[2] Y. Ishikawa, T. Nishikawa, T. Okada, S. Shinmura, Y. Kamado, F. Kanaya, and K. Wakino, "Mechanically tunable MSW bandpass filter with combined magnetic units," in *IEEE MTT-S Int. Microwave Symp. Dig.*, 1990, pp. 143–146.

[3] M. Makimoto and M. Sagawa, "Varactor tuned bandpass filters using microstrip-line ring resonators," in *IEEE MTT-S Int. Microwave Symp. Dig.*, May 1986, pp. 411–414.

[4] Y.-H. Shu, J. A. Navarro, and K. Chang, "Electronically switchable and tunable coplanar waveguide-slotline bandpass filters," *IEEE Trans. Microwave Theory Tech.*, vol. 39, pp. 548–554, Mar. 1991.

[5] I. C. Hunter and J. D. Rhodes, "Electronically tunable microwave bandpass filters," *IEEE Trans. Microwave Theory Tech.*, vol. MTT-30, pp. 1354–1360, Sept. 1982.

A Broad-Band Sleeve Monopole Integrated into Parallel-Plate Waveguide

Zhi Ning Chen, Kazuhiro Hirasawa, and Ke Wu

***Abstract*—In this paper, a sleeve monopole is proposed and studied theoretically and experimentally. It consists of a resonant loading and a conventional sleeve monopole vertically integrated in a parallel-plate waveguide. A modal expansion technique is used to model the induced currents over the monopole surface, and fields in the region of interest are characterized by cylindrical harmonic functions. A Fourier least-square integration is applied to find the expansion coefficients by the boundary and continuity conditions. A 5.8-GHz industrial-, scientific-, and medical-band example is selected for the studies. It is found that the new monopole exhibits a large bandwidth exceeding 37% for −10-dB return loss. Calculated results are validated by the measurements.**

***Index Terms*—Least-square integration, monopole, parallel-plate waveguide.**

I. INTRODUCTION

Geometrical simplicity, modal purity, and cost effectiveness make the coaxially fed monopoles a unique choice for a large variety of microwave devices and communication antennas. Generally, a simple coaxially fed monopole may be used as either an adapter or a feeder to a waveguide, and this engineering subject has been studied for a number of years [1]–[7]. If used as an adapter, the coaxially fed monopole realizes the transition from a coaxial line to other transmission-line systems such as rectangular or parallel-plate waveguides [5]–[7]. As a feeder, the monopole is useful for an antenna feeding network or a radial signal dividing/combining network of power amplifiers, e.g., in the design of direct broadcast satellite (DBS) planar receiving antennas [8], [9]. To broaden the limited impedance bandwidth of a monopole, some loading techniques were proposed, such as dielectric coatings [10], [11] and disc-ended or top-hat structures [2], [6], [7].

In this paper, a monopole with double sleeves and dielectric loading is presented for broad-band applications, integrated into a parallel-plate waveguide. A modal expansion technique has been developed to investigate the proposed monopole [11], [12]. To begin with, the region of interest between the parallel plates is divided into four subregions, where electric- and magnetic-field components are formulated subject

Manuscript received March 5, 1999. This work was supported by the Japan Society for the Promotion of Science Fellow Programs under a Monbusho Grant-in-Aid.

Z. N. Chen was with the Institute of Information Sciences and Electronics, University of Tsukuba, Tsukuba, Ibaraki 305-8573 Japan. He is now with the Centre for Wireless Communications, National University of Singapore, 117674 Singapore.

K. Hirasawa is with the Institute of Information Sciences and Electronics, University of Tsukuba, Tsukuba, Ibaraki 305-8573 Japan.

K. Wu is with Poly-Grames Research Center, Ecole Polytechnique, Montreal H3C 3A7, P.Q., Canada.

Publisher Item Identifier S 0018-9480(00)05475-2.

0018–9480/00$10.00 © 2000 IEEE

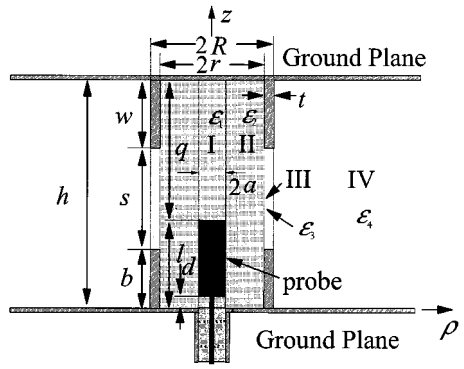

Fig. 1. Geometrical description and physical notation of the proposed double-sleeve monopole housed in a parallel-plate waveguide.

to the boundary conditions. Applying the boundary and continuity conditions with the field equations determines the expansion coefficients via a Fourier least-square integration. Subsequently, the induced currents on the monopole can be calculated. This analysis is validated by comparing results reported in [13] as well as our own experiments. Industrial, scientific, and medical (ISM) examples operating at 5.8 GHz are then selected to show the broadened impedance characteristics of the proposed monopole in the parallel-plate waveguide.

II. Theory and Formulation

The geometry of the proposed sleeve monopole is described in a cylindrical coordinate system (ρ, ϕ, z), as shown in Fig. 1. The spacing of the parallel plates is h and the length of the inner cylindrical conductor is l. The radii of the probe and dielectric jacket are denoted by r and a, respectively. b and w stand for the lengths of two metallic sleeves while t is the thickness of the two sleeves. The whole structure is partitioned into four subregions marked by dielectric constants ε_n with $n = 1, 2, 3, 4$ ($\varepsilon_n = \varepsilon_{rn}\varepsilon_0$). A small source region having its height d is designated with a uniform electric field, and its constant voltage source is V_0. Similar to the analytical procedure in [12], a modal expansion technique is used to formulate and investigate characteristics of the structure. For the sake of concision, this procedure is not described here.

Electric and magnetic fields in each subregion can be formulated in terms of an electric-type (TM^z) hertz potential [14]. Finite-series or truncated modal field expansions are developed as follows by considering the boundary conditions. For example, inside subregion II (dielectric jacket) with $r \geq \rho \geq a$ and $0 \leq z \leq h$, the fields are given by

$$\begin{cases} E_z^{\mathrm{II}}(\rho, z) \\ \quad = \dfrac{1}{j\omega\varepsilon_{r2}\varepsilon_0\mu_0}\displaystyle\sum_{n=0}^{N_2} k_{\rho 2n}^2\Big[a_{2n}J_0(k_{\rho 2n}\rho) + b_{2n}N_0(k_{\rho 2n}\rho)\Big] \\ \qquad \cdot\cos\left(\dfrac{n\pi}{h}z\right) \\ H_\phi^{\mathrm{II}}(\rho, z) \\ \quad = \dfrac{1}{\mu_0}\displaystyle\sum_{n=0}^{N_2} k_{\rho 2n}\Big[a_{2n}J_1(k_{\rho 2n}\rho) + b_{2n}N_1(k_{\rho 2n}\rho)\Big]\cos\left(\dfrac{n\pi}{h}z\right) \end{cases} \tag{1}$$

with $k_2^2 = \varepsilon_{r2}k_0^2$ and

$$k_{\rho 2n} = \pm\sqrt{k_2^2 - (n\pi/h)^2} = \begin{cases} \sqrt{k_2^2 - (n\pi/h)^2}, & k \geq 2(n\pi/h) \\ -j\sqrt{(n\pi/h)^2 - k_2^2}, & k_2 \leq (n\pi/h). \end{cases}$$

The terms a_{1n} and b_{1n} are unknown field expansion coefficients. In the above equations, $J_m(\cdot)$ and $N_m(\cdot)$ are, respectively, Bessel functions of the first and second kinds, having the order $m = 0$ or 1.

To determine the coefficients of field expansions, the remaining boundary and continuity conditions in connection with the tangential fields should be fulfilled. Usual field Fourier matching is applied by integration over the boundaries and interfaces of the regions. For example, at the interface of subregions I and II, the perfect electrically conducting (PEC) condition for electric fields (on the surface of the monopole) and the continuity condition for both electric and magnetic fields (on the remaining aperture) should be satisfied. As for the source region, a uniform field was assumed, i.e., $E_z^{\mathrm{II}}(\rho, z) = -V_0/d$ for $0 \leq z \leq d$. Similarly, by enforcing the conditions, a set of linear equations can be set up. Combining the linear equations then leads to a complex matrix system (2) of order $N_t = 2 \times N_2 + 2 \times N_3$, which is readily solved for the expansion coefficients in subregions II and III a_{2n}, b_{2n}, a_{3n}, and b_{3n}

$$\begin{bmatrix} [Z_{11}]_{N_2\times N_2} & [Z_{12}]_{N_2\times N_2} & [0]_{N_2\times N_3} & [0]_{N_2\times N_3} \\ [Z_{21}]_{N_3\times N_2} & [Z_{22}]_{N_3\times N_2} & [Z_{23}]_{N_3\times N_3} & [Z_{24}]_{N_3\times N_3} \\ [Z_{31}]_{N_2\times N_2} & [Z_{32}]_{N_2\times N_2} & [Z_{33}]_{N_2\times N_3} & [Z_{34}]_{N_2\times N_3} \\ [0]_{N_3\times N_2} & [0]_{N_3\times N_2} & [Z_{43}]_{N_3\times N_3} & [Z_{44}]_{N_3\times N_3} \end{bmatrix} \cdot \begin{bmatrix} [a_2]_{N_2\times 1} \\ [b_2]_{N_2\times 1} \\ [a_3]_{N_3\times 1} \\ [b_3]_{N_3\times 1} \end{bmatrix} = [V_0]_{N_t\times 1}. \tag{2}$$

Once the coefficients a_{2n} and b_{2n} become known, it can be straightforward to obtain the induced currents on the monopole through the relationship $I(z) = 2\pi aJ = 2\pi aH_\phi^{\mathrm{II}}(a, z)$, such that

$$I(z) = 2\pi aH_\phi^{\mathrm{II}}(a, z) = \frac{2\pi a}{\mu_0}\sum_{n=0}^{N_2} k_{\rho 2n}\Big[a_{2n}J_1(k_{\rho 2n}\rho) + b_{2n}N_1(k_{\rho 2n}\rho)\Big]\cos\left(\frac{n\pi}{h}z\right). \tag{3}$$

In addition, the input impedance can easily be evaluated by using $Z_{\mathrm{in}} = V_0/I(0)$ from (3).

III. Design, Results, and Discussion

Some features of the proposed sleeve monopole structure will be shown with an engineering design for 5.8-GHz ISM-band applications. A monopole structure is first modeled numerically and optimized such that a satisfactory impedance match can be obtained at the operating frequency with a possible broad bandwidth. Subsequently, the monopole is designed and fabricated in the consideration of an SMA connector with a long thin dielectric (Teflon) jacket and also a metallic tape sticking on a support (dielectric jacket). A 50-Ω coaxial line is used as a feeder. Two electrically large circular conducting plates are used to form an approximate radial parallel-plate waveguide. The lower sleeve is electrically connected to the bottom plate, while the other is attached to the upper plate. The dielectric jacket is short circuited at its ends by the plates. In our design, a large impedance bandwidth with the possible best match characteristics at 5.8 GHz is expected. With the SMA connector, the design freedom remains in changing the size of the sleeves and the spacing between the parallel plates. In fact, this consideration also simplifies the design procedure. Optimized dimensions of the structure are listed in Table I.

With reference to the criteria suggested in [12] and [13], we carry out numerical experiments to assess the accuracy of the model and

TABLE I
OPTIMIZED PARAMETERS AND GEOMETRICAL DIMENSIONS OF THE SELECTED EXAMPLE FOR OUR THEORETICAL AND EXPERIMENTAL STUDIES

h (mm)	w (mm)	b (mm)	l (mm)	r (mm)	d (mm)	a (mm)	t (mm)	ε_{r1}	ε_{r2}	ε_{r3}	ε_{r4}
47.0	17.0	11.80	21.90	2.057	0.03	0.318	0.28	1.0	2.08	1.0	1.0

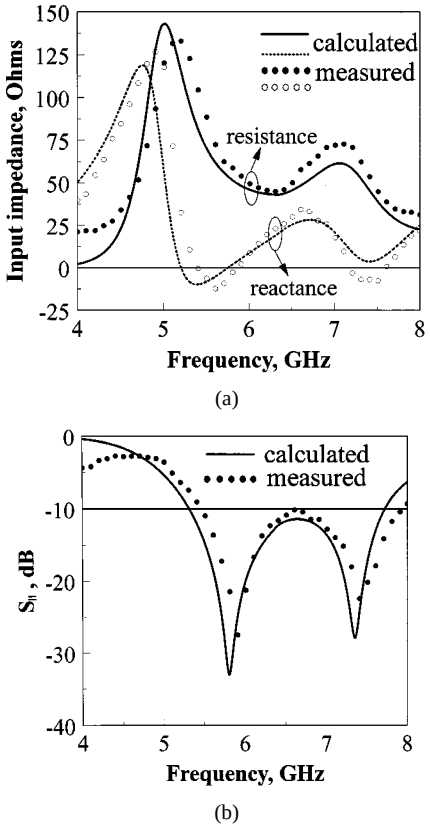

Fig. 2. Comparison of calculated and measured results of our 5.8-GHz monopole example (see Table I and Fig. 1 for its dimensions and physical description). (a) Input impedance. (b) Return loss S_{11}.

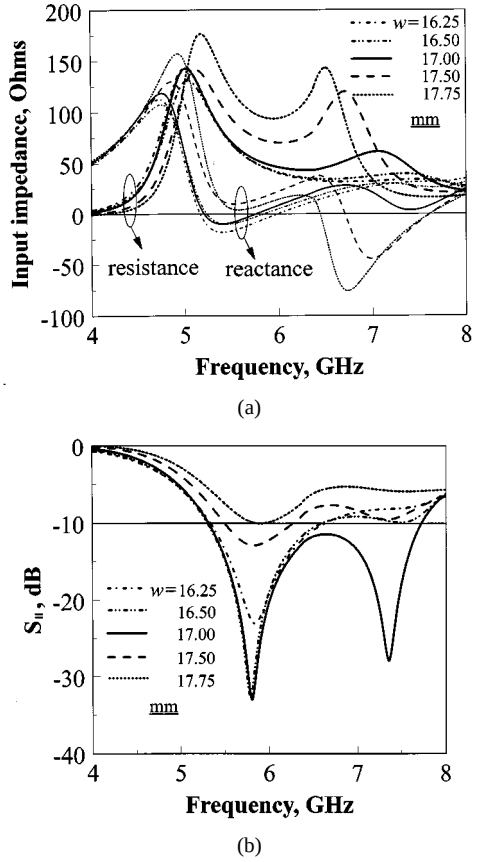

Fig. 3. Calculated frequency responses of the proposed monopole for different length w of the second sleeve (refer to Table I for other dimensions) with: (a) input impedance and (b) return loss S_{11}.

also to determine the number of modal expansions. As a result of the tradeoff between modeling accuracy and computational time, it is recommended to use a limited number of modes in the modeling, although results are, in principle, more accurate with more modes. Thus, the number of expansion terms $N = 60$ are selected in our calculations. The central processing unit (CPU) time at each frequency point is less than 6 s on a PC Pentium II (400 MHz).

To validate our model, the input impedances of a simple monopole ($w \to 0$, $b \to 0$, $\varepsilon_{r2} = 1.0$, and $h = 2.1\lambda_o$) and a conventional sleeve antenna ($w \to 0$, $\varepsilon_{r2} = 1.0$, $b = 0.25\lambda_o$, and $h = 2.1\lambda_o$) are calculated and compared with the experimental and modeling results given in [12] and [13], respectively. They agree very well for both of the special cases. Further, the proposed sleeve monopole at 5.8 GHz is tested. The calculated and measured input impedances and the return loss S_{11} are shown in Fig. 2. A good agreement is observed over 4–8 GHz, considering some mechanical tolerance. From Fig. 2(a), it is seen that a resonant loading causes one parasitic resonance. Large reactance between two modes is effectively cancelled out when the parasitic mode moves close to the first mode. Therefore, a 37% impedance bandwidth for $S_{11} < -10$ dB has been achieved by exciting two adjacent modes, as shown in Fig. 2(b).

As the second sleeve is the key ingredient in this new proposal, Fig. 3 shows calculated input impedance versus frequency in the presence of the second sleeve with a different length w, where other dimensions are fixed. The results show that the input resistance in the operating range increases significantly as the length w is extended. The input impedance in Fig. 3 demonstrates that the first resonance stems from the conventional sleeve monopole and the second from the parasitic sleeve. A modeling for the monopole without the second sleeve indicates that the second resonance gradually disappears as the length w tends to be zero. The calculated S_{11} shows the significant influence of the length w on the impedance match.

Fig. 4 displays frequency responses of the input impedance and S_{11} as a function of the spacing q. It can be seen that increasing the spacing q pushes the second resonant frequency up; however, the first frequency remains almost intact. The same reason as that for the length w is applied in this case. On the other hand, increasing the spacing q means a reduction in the ratio of the radius to the height of the dielectric resonator, which usually leads to the increases in resonant frequency. This suggests that the size of the jacket as well as the length w largely affect

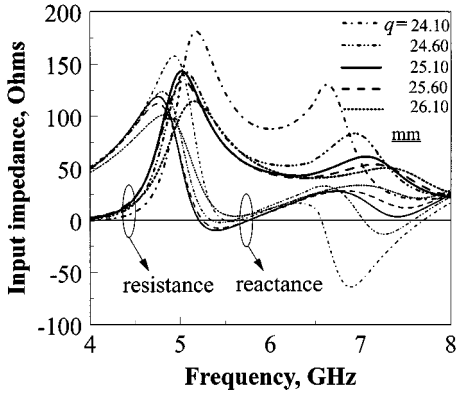

(a)

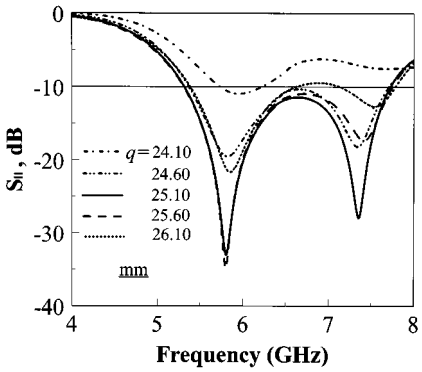

(b)

Fig. 4. Calculated frequency responses of the proposed monopole for different spacing q (refer to Table I for other dimensions) with: (a) input impedance and (b) return loss S_{11}.

characteristics of the second sleeve, which can be considered as part of the dielectric jacket.

Besides the width w and the spacing q, the parametrical studies on other parameters including the radius r of the sleeve, the sleeve length b and thickness t, and dielectric constant ε_{r2} are also conducted. The investigations show that the impedance characteristics of the proposed monopole are sensitive to the geometric dimensions and electrical parameters.

IV. Conclusion

A novel sleeve monopole integrated into a parallel-plate waveguide has been presented experimentally and investigated theoretically by a modal expansion modeling technique. The analysis indicates that this novel structure features a remarkably broad impedance bandwidth. A design example of 5.8-GHz ISM-band applications is used to showcase the underlying features of the proposed monopole. Our paper indicates that the performance of the monopole can effectively be improved by introducing the second sleeve that operates as a parasitic resonant loading. The parasitic resonance due to the second sleeve results in better matching condition and broader impedance bandwidth. Owing to its attractive technical merits, namely, simple geometry, low cost, and good characteristics, this structure shows promising applications in the design of broad-band adapters and feeders for microwave circuits and antennas.

References

[1] A. G. Williamson and D. V. Otto, "Coaxial fed hollow monopole in a rectangular waveguide," *Electron. Lett.*, vol. 9, pp. 218–220, Feb. 1973.
[2] M. E. Bialkowski, "Analysis of disc-type resonator mounts in parallel plate and rectangular waveguide," *AEU*, vol. 38, pp. 306–310, 1984.
[3] ——, "Probe antenna in arbitrarily terminated rectangular waveguide," *AEU*, vol. 39, pp. 190–192, 1985.
[4] B. Tomasic and A. Hessel, "Electric and magnetic current sources in the parallel plate waveguide," *IEEE Trans. Antennas Propagat.*, vol. AP-35, pp. 1307–1310, Nov. 1987.
[5] R. B. Keam and A. G. Williamson, "Analysis of a general coaxial-line/radial-line region junction," *IEEE Trans. Microwave Theory Tech.*, vol. 41, pp. 516–520, Mar. 1993.
[6] M. E. Bialkowski, "Analysis of a coaxial-to-waveguide adaptor including a descended probe and a tuning post," *IEEE Trans. Microwave Theory Tech.*, vol. 43, pp. 344–349, Feb. 1995.
[7] ——, "Modeling of a coaxial-to-waveguide power combining structure," *IEEE Trans. Microwave Theory Tech.*, vol. MTT-34, pp. 937–942, Sept. 1986.
[8] N. Goto and M. Yamamoto, "Circularly polarized radial line slot antennas," Inst. Elect. Inform. Commun. Eng., Toyko, Japan, Tech. Rep. AP-80-57, p. 43, Aug. 1980.
[9] P. W. Davis and M. E. Bialkowski, "Experimental investigations into a linearly polarized radial slot antenna for DBS TV in Australia," *IEEE Trans. Antennas Propagat.*, vol. 45, pp. 1123–1129, July 1997.
[10] M. E. Bialkowski, "Analysis of a coaxial-to-waveguide adaptor incorporating a dielectric coated probe," *IEEE Microwave Guided Wave Lett.*, vol. 1, pp. 211–214, Aug. 1991.
[11] K. W. Leung, Z. N. Chen, K. M. Luk, and E. K. N. Yung, "On the probe-fed dielectric resonator inside the parallel-plate waveguide," *IEEE Trans. Microwave Theory Tech.*, vol. 47, pp. 1113–1117, July 1999.
[12] M. A. Morgan, R. C. Hurley, and F. K. Schwering, "Computation of monopole antenna currents using cylindrical harmonics," *IEEE Trans. Antennas Propagat.*, vol. 38, pp. 1130–1133, July 1990.
[13] Z. Shen and R. H. MacPhie, "Rigorous evaluation of the input impedance of a sleeve monopole by modal-expansion method," *IEEE Trans. Antennas Propagat.*, vol. 44, pp. 1584–1591, Dec. 1996.
[14] R. F. Harrington, *Time-Harmonic Electromagnetic Fields*. New York: McGraw-Hill, 1961.